Macromolecules

Volume 40, Number 24 November 27, 2007

Review

How Nano Are Nanocomposites?

Dale W. Schaefer*,† and Ryan S. Justice†,‡

Department of Chemical and Materials Engineering, University of Cincinnati, Cincinnati, Ohio 45221-0012, and Materials and Manufacturing Directorate, Air Force Research Laboratory, WPAFB, Ohio 45433-7750

Received February 10, 2007; Revised Manuscript Received August 22, 2007

ABSTRACT: Composite materials loaded with nanometer-sized reinforcing fillers are widely believed to have the potential to push polymer mechanical properties to extreme values. Realization of anticipated properties, however, has proven elusive. The analysis presented here traces this shortfall to the large-scale morphology of the filler as determined by small-angle X-ray scattering, light scattering, and electron imaging. We examine elastomeric, thermoplastic, and thermoset composites loaded with a variety of nanoscale reinforcing fillers such as precipitated silica, carbon nanotubes (single and multiwalled), and layered silicates. The conclusion is that large-scale disorder is ubiquitous in nanocomposites regardless of the level of dispersion, leading to substantial reduction of mechanical properties (modulus) compared to predictions based on idealized filler morphology.

1. Introduction

Polymer nanocomposites are two-phase systems consisting of polymers loaded with high-surface-area reinforcing fillers.[1] Such systems have attracted enormous interest from the materials community because they theoretically promise substantial improvement of mechanical properties at very low filler loadings. In addition, nanocomposites are compatible with conventional polymer processing, thus avoiding costly layup required for the fabrication of conventional fiber-reinforced composites. The appeal of nanocomposites is illustrated by considering single-walled carbon nanotubes (SWCNTs). With tensile moduli in the terapascal range[2] and lengths exceeding 10 μm, simple composite models predict order-of-magnitude enhancement in modulus at loadings of less than 1%.

Introductory paragraphs similar to the above can be found in hundreds of nanocomposite papers. With the exception of reinforced elastomers, nanocomposites have not lived up to expectations. Although claims of modulus enhancement by factors of 10 exist, these claims are offset by measurements that show little or no improvement. At this point we restrict our attention to the impact of nanoscale fillers on composite modulus. Modulus enhancement depends on intrinsic properties of matrix and filler as well as interactions between matrix and filler. Ultimate properties, on the other hand, are more sensitive to defects, a topic beyond the scope of this review.

The lackluster performance of nanocomposites has been attributed to a number of factors including poor dispersion, poor interfacial load transfer, process-related deficiencies, poor alignment, poor load transfer to the interior of filler bundles, and the fractal nature of filler clusters.[3] That said, not all nanocomposites have underperformed on the basis of industrial standards. Indeed, carbon-black-filled organic rubber is one of the premier materials engineering successes of the 20th century. Currently, colloidal silica (precipitated silica) is displacing carbon black as the filler of choice, especially for high-performance applications such as tire treads.[4] Filler morphology

* Corresponding author: Tel +1-513-556-5431; Fax +1-206-600-3191; e-mail dale.schaefer@uc.edu.
† University of Cincinnati.
‡ Air Force Research Laboratory.

10.1021/ma070356w CCC: $37.00
Published on Web 11/01/2007

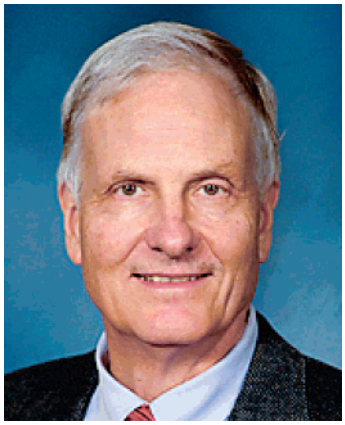

Dale W. Schaefer is Professor of Chemical and Materials Engineering at the University of Cincinnati. He received his Ph.D. in Physical Chemistry at M. I. T. and did postdoctoral studies in the Department of Physics at M. I. T. Dr. Schaefer previously served as a technical manager at Sandia National Laboratories, a Senior Technical Advisor at the Department of Energy, and Dean of Engineering at the University of Cincinnati. He is a Fellow of the American Physical Society and the American Institute of Chemists. In 2004, he was the John Wheatley Scholar at Los Alamos National Laboratory. In 2005 and 2007, he was a visiting scientist at the Institute of Chemistry, Chinese Academy of Sciences. Prof. Schaefer's research interests span the physics and chemistry of colloids, polymers, and ceramics. He is a specialist on structure–property relationships in complex materials, which he studies using light, X-ray, and neutron scattering.

Ryan S. Justice is a Ph.D. candidate at the University of Cincinnati. Mr. Justice currently serves as a Materials Engineer in the Materials and Manufacturing Directorate at Wright Patterson Air Force Base. His dissertation research involves using small-angle scattering to elucidate the hierarchical morphology/property relationships of nanocomposite fillers. In 2004, Mr. Justice received the American Society for Materials A. E. Focke Engineering Award for the "graduate student best exemplifying professional and ethical engineering attributes". In 2006, he won the Margaret C. Etter Student Lecturer Award from the Small-Angle Scattering Special Interest Group of the American Crystallographic Association. In 2007, he received the Outstanding Graduate Student in Research Award from the Department of Chemical and Materials Engineering at the University of Cincinnati. Mr. Justice obtained his B.S. in Biomedical Engineering from Wright State University, Dayton, OH, and his M.S. in Chemical and Materials Engineering from the University of Cincinnati.

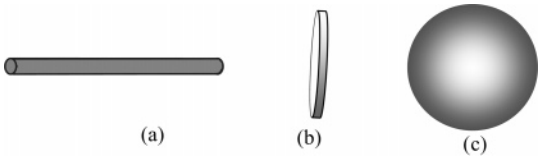

Figure 1. Schematics of (a) 1-dimensional, (b) 2-dimensional, and (c) 3-dimensional colloidal particles.

is a key factor that explains the commercial success of soft nanocomposites and the marginal performance of hard nanocomposites, a point developed in subsequent paragraphs.

When considering the relationship between morphology and mechanical properties of nanocomposites, sorting out potential compromising factors is not easy. For example, in a system using carbon nanotubes as the filler, a typical strategy to address load transfer between the matrix and filler is to functionalize the nanotube surface with a coupling agent. Such modification, however, introduces defects on the nanotubes and also alters the propensity of the filler to disperse in the matrix, both of which influence mechanical properties in ways similar to the influence of interfacial bonding. Thus, it is difficult to isolate the effect of functionalization on load transfer.

Simplified schematics (cartoons) have played a central role in nanocomposite research, particularly regarding the impact of morphology on properties. Figure 1, for example, shows idealized one-, two-, and three-dimensional colloidal particles. Examples include one-dimensional carbon nanotubes, two-dimensional layered silicates, and three-dimensional Stöber silica spheres. Such representations are helpful when analyzing nanocomposite properties. Low-dimensional fillers, for example, are more difficult to disperse than their three-dimensional cousins. The difference arises because three-dimensional, quasi-spherical particles touch at a point, whereas one-dimensional rods or tubes can contact along a line, thus leading to enhanced particle interaction. Two-dimensional sheets offer even larger contact area. As a result of these enhanced interactions, layered silicates exist naturally as stacks and carbon nanotubes form ropelike networks with side-by-side packing. Stacking and side-by-side packing lead to enhanced van der Waals attraction accounting for the propensity of low-dimensional colloids to cluster. On the basis of the cartoons, therefore, one expects that spherical particles would be easier to disperse than either rods or sheets. This prediction is borne out. The cartoons, therefore, properly suggest that low-dimensional colloids are difficult to disperse.

Cartoons can also mislead regarding filler morphology. As we will show, the morphology of nanocomposites is actually substantially more complex than the cartoons suggest. Even well-dispersed nanofillers naturally aggregate to form clusters whose size extend to length scales exceeding 1 μm. The presence of large-scale aggregates is not widely acknowledged in the nanocomposites literature, primarily because such aggregates are difficult to detect by electron microscopy, the predominant characterization technique of the nanocomposites community. Optimism regarding the degree of dispersion may also affect the interpretation of electron images. Fortunately, ultra-small-angle scattering readily reveals the large-scale morphology of nanocomposites.

With these concepts in mind, we will examine the morphology of nanoscale reinforcing fillers as measured both by scattering and imaging. On the basis of morphological considerations alone, one can qualitatively understand the range of systems and properties where nanocomposites offer performance improvement. We will explore one-dimensional, two-dimensional, and three-dimensional fillers in water suspensions, in soft matrices, and in hard matrices. Suspensions are included because light scattering is difficult for solid samples (due to surface scattering), so our understanding of the 10 μm scale morphology of colloidal fillers is largely based on suspensions.

This paper is not an attempt to review the immense literature on nanocomposites, as numerous such reviews already exist.[1,4–17]

Rather, we focus on the relationship between morphology of the reinforcing phase and the mechanical properties of the resulting composite. We take the position that the large-scale aggregated character of nanoscale fillers is the most important factor that compromises nanocomposite mechanical performance. Unless the aggregation is mitigated, interface modification, improved processing, more rigorous dispersion, higher native aspect ratio, and better morphology control will not lead to the lofty performance improvements once predicted.

2. Morphological Characterization: Imaging vs Scattering

Electron microscopic imaging (real-space analysis) is in principle more powerful than small-angle scattering (SAS, reciprocal-space analysis) for elucidating nanoscale morphologies. The main reason is phase information is lost in scattering, so one cannot uniquely determine structure. That is, more than one morphology may account for the observed scattering. Although the loss of phase information seems at first sight to be a severe limitation, the loss can, in some cases, be beneficial.[18]

To illustrate the relationship between real- and reciprocal-space analysis, we define structure as the electron density distribution, $\rho(\mathbf{r})$, as a function of position, $\mathbf{r}$. If we knew $\rho(\mathbf{r})$, we would know the position of every atom in the sample. In principle, by tomographic imaging one could measure $\rho(\mathbf{r})$ and definitively determine structure. Tomographic imaging, however, is an arduous procedure requiring thin sample sectioning. Thus, the direct measurement of $\rho(\mathbf{r})$ is seldom done. Even in cases where $\rho(\mathbf{r})$ is measured, it is difficult to resolve structures smaller than 1 μm. More importantly, $\rho(\mathbf{r})$ depends on the portion of the sample in the beam; i.e., if you move the sample in space, $\rho(\mathbf{r})$ changes. The ability to select images that match a specific operator's prejudices is a manifestation of the spatial dependence of $\rho(\mathbf{r})$.

The fact is that for disordered systems $\rho(\mathbf{r})$ contains too much information to be conceptually useful. What is needed is an appropriate statistical or ensemble average, $\langle ... \rangle$, of $\rho(\mathbf{r})$. A simple spatial average will not do the job since $\langle \rho(\mathbf{r}) \rangle$ is simply the mean density. What is needed is not an average over the absolute position of the atoms, but an average of the correlations among those positions. The correlation function, $\Gamma_\rho(r)$, is the simplest quantity that measures spatial correlations:

$$\Gamma_\rho(r) = \int \rho(\mathbf{u})\, \rho(\mathbf{u} + \mathbf{r})\, \mathrm{d}\mathbf{u} \tag{1}$$

For an isotropic system $\langle \Gamma_\rho(r) \rangle$ is a scalar quantity that depends only on the relative position of the atoms. $\langle \Gamma_\rho(r) \rangle$ can be compared to morphological models in a quantitative fashion.

This correlation function is called the Paterson function in the X-ray diffraction community.[19] The Fourier transform of the Paterson function is exactly what is measured in an X-ray scattering experiment. The scattered intensity, $I(q)$, is

$$I(q) \propto \int \langle \Gamma_\rho(r) \rangle \mathrm{e}^{-i\mathbf{q}\mathbf{r}}\, \mathrm{d}r \tag{2}$$

where q is related to scattering angle (θ) by $q = 4\pi/\lambda \sin(\theta/2)$, with λ being the wavelength of the radiation. Based on this Fourier transform, r and q are conjugate variables.

Although eqs 1 and 2 are equivalent Fourier transform pairs, it is more common to extract morphological information in reciprocal space using eq 2 than in real space using eq 1. We know of no examples $\Gamma_\rho(r)$ was calculated for nanocomposites from real-space imaging data. Incidentally, calculating $\Gamma_\rho(r)$ from $\rho(\mathbf{r})$ is equivalent to throwing out the phase information, which happens in a scattering experiment inherently. Thus, real-space imaging analysis ends up equivalent to reciprocal-space scattering analysis. It is, however, much easier to obtain the data in reciprocal space.

In order to fully sort out the structure of a complex, disordered system, both imaging and scattering are necessary. Each technique acts as a check on the other by complementing the other's deficiencies. For instance, some models that are consistent with scattering data can be ruled out from the imaging information. Scattering from Gaussian polymer coils, for example, is very similar to scattering from randomly oriented thin disks. In contemporary language, coils and disks have the same fractal dimension. The difference between coils and disks, however, is readily apparent via imaging. Images, on the other hand, are difficult to quantify, they are subject to operator selectivity, and they are often susceptible to compromise by sample preparation. All of these limitations are minimized in the world of scattering.

3. Nanocomposite Fillers

3.1. Aggregated Spheroidal Fillers. 3.1.1. Morphology of Precipitated Silica. To illustrate the interplay of imaging and scattering data, consider the data in Figure 2.[20] The precipitated silica[4] in Figure 2 is a new generation material produced from porcellanite, a mineral rich in amorphous silica that is found in the Negev desert in southern Israel (Dimosil 288, Dimona Silica Industries, Beer Shiva, Israel). The amorphous character of porcellanite is conducive to an efficient synthetic process that yields silica with specific surface areas in the range of 100−400 m^2/g. Dimosil 288 in Figure 2 has a BET surface area of 170 m^2/g.

Figure 2a is a transmission electron microscopy (TEM) image showing the primary structural building block of precipitated silica is a quasi-spherical particle ~200 Å in diameter. These so-called primary particles are aggregated into a large-scale disordered secondary structure. It is difficult to say much more about the morphology based on the TEM image. Neither the size nor the structure of the aggregates is evident.

A richer picture of the morphology emerges from the scattering data in Figure 2b, which compares scattering (light + X-ray) from a wet suspension taken directly from the synthesis reactor and the same material after room temperature drying. The dry sample shows four structural levels, the scale of which can be read off the plot as roughly π/q_t, where q_t is the value of q at the transition region between the power-law regions.[21] The power-law regions show up as linear on the log−log plot. The values of the four length scales shown in the plot were actually determined from a more sophisticated unified data analysis method that breaks the curve into Guinier and Porod regions, where "Guinier" refers to the transitions and "Porod" refers to the power-law regions.[22] Using this Guinier−Porod approach, the length scales turn out to be the radii of gyration (R_gs) of the structural features. Andre Guinier first demonstrated that the size of colloidal particles could be extracted from small-angle scattering (SAS) data.[23] Porod first showed that the surface area of a colloid could be calculated from the scattered intensity in the power-law regime.[24]

The presence of four-length scales (i.e., four transition regions) shown in Figure 2b implies a hierarchical morphology consisting of primary particles (R_g = 126 Å) clustered into aggregates (R_g = 3000 Å). These aggregates are further clustered into two classes of agglomerates referred to in this work as "hard" (R_g = 3.5 μm) and "soft" (R_g = 44 μm). Note that the 44 μm soft agglomerate feature is not present in the wet sample

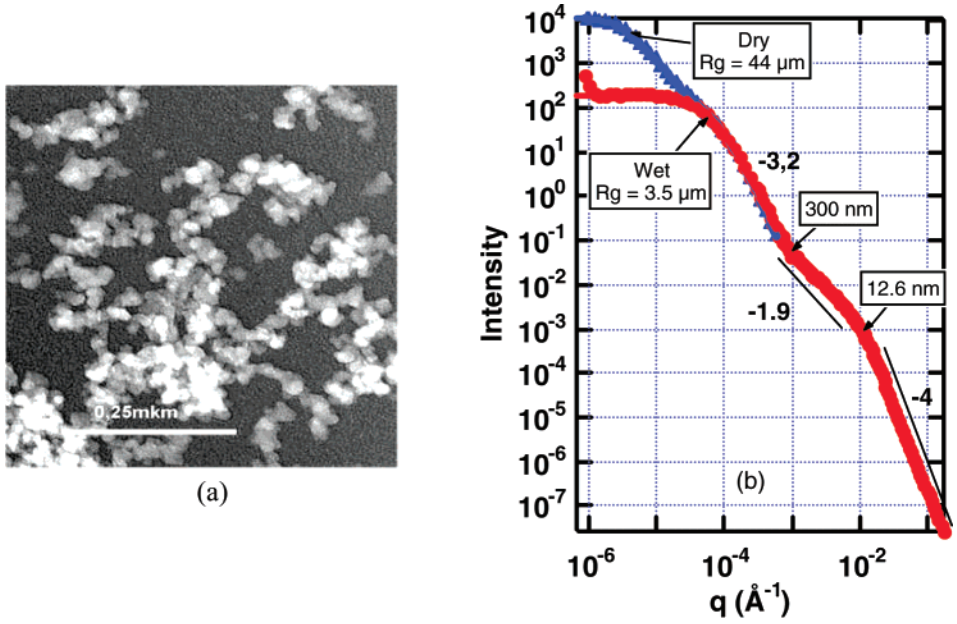

Figure 2. (a) TEM of Dimosil precipitated silica.[20] The scale bar is 0.25 μm. (b) Combined light and ultra-small-angle X-ray scattering (USAXS) data for Dimosil precipitated silica in the wet and dried states. The dry data show four levels of structure whereas the wet sample shows only three levels. The limiting slope of −4 is due to the smooth surface of the primary particles. The TEM image is consistent with smooth-surfaced primary particles, although it would be difficult to eliminate short-scale roughness based on the image.

data, which shows that these structures develop during drying.[25] The designation "hard" and "soft" is based on sonication studies (not shown). If a suspension of the dried product is subjected to intense ultrasonic perturbation, the 44 μm feature disappears from the scattering profile, whereas the 3.5 μm feature persists. Thus, the former is soft and the latter is hard.

When considering the reinforcement of rubber, optimization of the aggregate and agglomerate morphology is the key to effective reinforcement.[21,26] Large-scale agglomerates are nonreinforcing and must be broken down or dispersed during fabrication to achieve effective modulus enhancement. Therefore, the presence of soft agglomerates is desirable. Among the available grades of precipitated silicas we have studied, 3.5 μm is the smallest hard agglomerate we have found, which accounts for the highly dispersing character of Dimosil 288.

To appreciate the importance of morphology on reinforcement, it is necessary to examine the internal structure of aggregates and agglomerates. Such clusters (the delineation of "cluster" refers to both aggregates and agglomerates) usually display fractal geometry. Fractal geometry is a method to characterize common types of disordered objects. If N is the number of subunits in a cluster (e.g., for aggregates, the number of primary particles within the aggregate), the mass fractal dimension, d_m, is defined by the power-law relationship

$$N \sim R^{d_m} \tag{3}$$

where R is some measure of the cluster size. In this simple analysis, polydispersity is neglected. Note that eq 3 is also appropriate to conventional nonfractal Euclidian objects, in which case d_m is the object's conventional dimension. The objects in Figure 1, for example, obey eq 3 with $d_m = 1$, 2, and 3, corresponding to rods, disks, and spheres. Non-Euclidean objects that obey eq 3 are called mass fractals although the term mass fractal is often applied to any object, including rods, disks, and spheres, that obeys eq 3.

In reciprocal space, mass-fractal objects follow a power-law relationship conjugate to eq 3, which is the reason why the data in Figure 2b are plotted on log−log axes. Specifically the scattered intensity becomes

$$I(q) \sim \frac{B}{q^{d_m}} \qquad 1 \le d_m < 3 \tag{4}$$

Thus, a one-dimensional randomly oriented rod gives a power-law scattering profile with a slope of −1, and a disk or sheetlike object gives a slope of −2. For a three-dimensional object, eq 4 does not apply. In this case the slope turns out to be −4 if the object's surface is smooth (surface scattering is treated below). One can easily distinguish rods, disks, and spheres on the basis of whether the slope of log $I(q)$ vs log q is −1, −2, or −4. The fact that the large-q data in Figure 2b follow a power-law with an exponent of −4 shows that the surfaces of the 126 Å primary particles are smooth. The −4 power-law exponent is called Porod's law. B is a power-law prefactor, which is very significant in the analysis of scattering data, but beyond the realm of this review.

Application of eq 4 to Figure 2b at $q = 0.003$ Å^{-1} reveals that the 3000 Å aggregates have a noninteger or fractional dimension ($d_m = 1.9$), which is why such objects are called "fractals". Fractal dimensions between 1.7 and 2.1 are typical for clusters formed by kinetic growth processes.[27] Kinetic growth refers to situations where a system evolves far from equilibrium. When aggregates form by irreversible sticking of primary particles, the system never reaches equilibrium; thus, the growth is kinetic. In the synthesis of precipitated silica, aggregates form by kinetic aggregation soon after the 120 Å primary particles.[28]

Scattering in the power-law region associated with the 3.5 μm hard agglomerates is not consistent with eq 4 since the power-law slope is −3.2. The hard agglomerates, therefore, are not mass fractals. From the slope of −3.2, we can infer that the agglomerates are uniformly dense objects (i.e., $d_m = 3$) with a rough surface. These objects are almost certainly porous, but they are still uniformly dense on dimensional scales exceeding the aggregate size of 3000 Å.

Surface roughness is quantified by a surface fractal dimension, d_s, which relates the surface area, S, to the object's size, $S \sim$

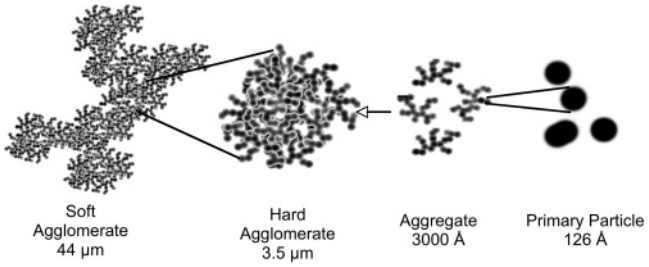

Figure 3. Schematic of the morphology of precipitated silica.[21] Four levels of structure are observed. Note that the primary particle and hard agglomerate are both uniformly dense, but the former is compact and smooth-surfaced whereas the latter is porous and rough-surfaced. The morphologies of the aggregate and soft agglomerate are statistically very similar, except for the nature of the buliding block. Primary particles make up the aggregate whereas hard agglomerates make up the soft agglomerate. This figure is a schematic, not a simulation.

R^{d_s}. Objects obeying this equation are called surface fractals. When roughness is taken into account, eq 4 generalizes to

$$I(q) \sim \frac{B}{q^{2d_m - d_s}} \qquad 1 \le d_m \le 3, 2 \le d_s \le 3 \tag{5}$$

For a mass fractal $d_m = d_s$ so eq 5 reduces to eq 4. For a uniformly dense (non mass-fractal) object $d_m = 3$, so $I(q) \sim q^{-(6-d_s)}$. Using this relationship, we conclude that the 3.5 μm agglomerates are uniformly dense globules with a rough surface of surface dimension $d_s = 2.8$. Such a high surface dimension means that the surface is very rough as depicted by the schematic of the hard agglomerate in Figure 3. The process by which hard agglomerates form is not known, although we do know they form after the aggregates.[29] Note that when $d_m = 3$ and $d_s = 2$, corresponding to a uniformly dense, smooth-surfaced object, $I(q) \sim q^{-4}$, which is, as mentioned above, Porod's law.

When power-law analysis is applied to the soft agglomerates in the region around $q = 10^{-5}$ Å^{-1}, one finds $d_m \cong 2$, also consistent with kinetically limited agglomeration. Apparently, secondary agglomeration occurs during drying, since 44 μm soft agglomerates are not present in the wet sample. The building blocks of the soft agglomerates are the 3.5 μm hard agglomerates, so N in eq 3 refers to the number of hard agglomerates in one soft agglomerate.

Armed with the above information, we can now construct a more realistic schematic of the morphology of Dimosil 288 precipitated silica (Figure 3) than is obvious from the TEM in Figure 2a. From the scattering data, two new levels of morphology emerge (soft and hard agglomerates), the nature of which is critical to dispersion and to the properties of silica-filled rubber. On the other hand, without TEM the idea of using fractal analysis to quantify the morphology would never have come up. It was TEM images showing disordered colloidal aggregates that spurred the analysis of such structures using fractal concepts.

3.1.2. Silica Morphology and Mechanical Properties. The presence of aggregated structures has profound implications for reinforcement. For unaggregated, isolated, rigid spheres, Smallwood[30] predicts that the enhancement of the modulus is independent of the size of the filler particles and is linearly related to loading in the limit of low loading. Specifically, if E_c is the Young's modulus of the composite and E_m is the Young's modulus of the matrix, the modulus enhancement, E_δ, is particularly simple:[30]

$$E_\delta = \frac{E_c}{E_m} = 1 + 2.5\phi, \quad \phi \ll 1 \tag{6}$$

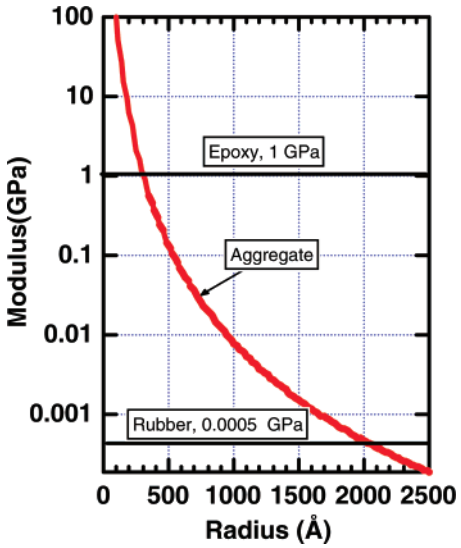

Figure 4. Dependence of the modulus of a fractal aggregate on the aggregate size. For comparison, typical moduli of hard and soft matrices are shown. When the modulus of the aggregate falls below that of the matrix, there is no reinforcing effect. The chemical exponent, c, is assumed to be 1.1, characteristic of reaction-limited cluster aggregates. The fact that this dimension is near unity means that the spanning arms are close to linear (i.e., the spanning path is not tortuous). The radius of the spanning arm is 100 Å, and the Young's modulus of the arm material is 100 GPa.

where ϕ is the volume fraction filler. In this rigid filler limit, the elastic energy is stored in the distorted strain field around the particles. The Smallwood analysis assumes no alteration of the matrix elastic properties due to the filler. Sternstein and Zhu, however, provide considerable evidence that polymer−filler interactions lead to labile cross-links in the vicinity of the filler, which leads to a larger modulus increment at finite strain rates than predicted by eq 6.[31,32]

For the case of aggregated fillers, no rigorous theory of reinforcement exists. Witten, Rubinstein, and Colby (WCR) however provide insight into reinforcement by fractal aggregates.[33] These authors assume that the elastic energy is stored in the spanning arms of the filler itself. The stiffness of the aggregate (and therefore the amount of stored energy) depends on the tortuosity of the connected spanning path. The tortuosity is characterized by a new fractal dimension, c, which relates the number of primary particles (L/a) in the spanning path to the cluster size, R:

$$\frac{L}{a} \cong \left(\frac{R}{a}\right)^c \tag{7}$$

where L is the length of the spanning path and "a" is the corresponding size of the primary particles. If $c = 1$, the spanning path is linear. The modulus of the aggregate, E_{agg}, is related to c as

$$E_{agg} \cong E_f\left(\frac{a}{R}\right)^{3+c} \tag{8}$$

where E_f is the Young's modulus of the bulk filler material (~100 GPa for silica).

Equation 8 shows that the aggregate modulus drops precipitously with aggregate size R, as shown in Figure 4. It must be recognized that eq 8 is based on a scaling argument, so absolute numbers are order-of-magnitude. Nevertheless, Figure 4 shows that aggregate structures are ineffective at reinforcing hard materials since the aggregate modulus falls below that of the

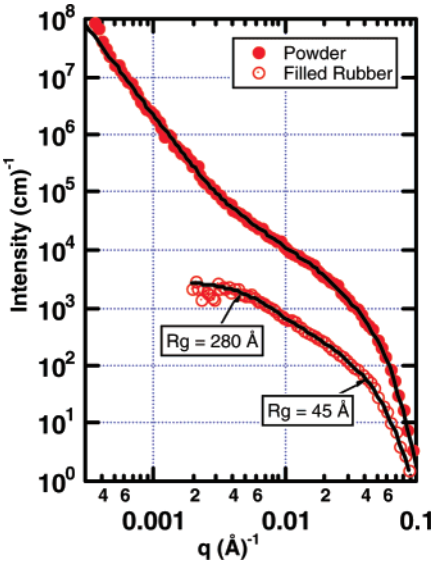

Figure 5. USAXS scattering profile for precipitated silica as a dry powder and compounded into styrene−butadiene rubber.[29] The primary particle radius of 45 Å and aggregate radius of 280 Å are consistent with both curves. In the filled rubber, however, scattering from the agglomerate is not observed. An air background was subtracted from the powder, and an unfilled rubber blank was subtracted from the filled rubber data. The loading is 11.7 wt % silica. No colloids other than the silica filler were included in the formulation of the rubber.

matrix for cluster sizes comparable to that of the primary particles. This analysis gives the first clue as to the limited modulus enhancement of thermosets reinforced with nanoparticles. We will return to this point after discussing the morphology of carbon nanotubes.

A macroscopic analogue of the effect captured by WRC is the difference between steel and steel wool. Steel is a high-modulus material so it is reasonable to expect that loading of a composite with steel fibers would lead to considerable stiffening. Steel wool, however, is soft, and expected reinforcement with steel wool would be much less than aligned steel fibers. Filler aggregates, like entangled carbon nanotubes discussed below, are morphologically similar to steel wool.

Some evidence supporting the WRC model is found in Figure 5, which compares the scattering profiles for a precipitated silica powder and an organic rubber reinforced with the same filler. The filler and rubber were made following Schaefer and Chen,[28] with the exception that a silane coupling agent was used to modify the filler surface during precipitation.[29] The data show that the agglomerate scattering is reduced in the filled rubber. The high-shear forces active during compounding break up the agglomerates leaving the aggregates, which are small enough to withstand the compounding shear.

The WRC model predicts an unusual power-law tensile stress (σ)−deformation (λ) curve at high deformation:

$$\sigma \sim \lambda^s \tag{9}$$

Figure 6 shows tensile data for precipitated silica in organic rubber. The data display a limited region of power-law behavior with an exponent of 2.9. WRC predict s values between 0.9 and 21, dependent upon assumptions regarding deformation of the aggregate. The value of 2.9 is more consistent with the analysis that assumes that the elastic energy is primarily stored as lateral compression of the aggregate, which occurs as the aggregate is strongly stretched in tension. At low deformation the exponent, *s*, is much larger, which could be due to tensile

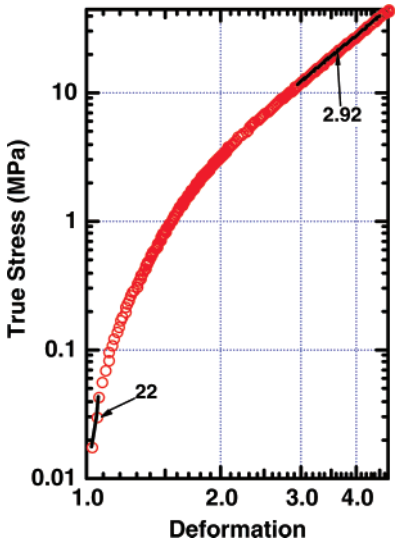

Figure 6. Stress−deformation curve for the silica-filled rubber sample in Figure 5.[28] The data show a small region of power-law behavior as predicted by Witten, Rubinstein, and Colby.[33] The slope at small strain is more consistent with tensile deformation of the aggregate assuming strong contacts between aggregates.

deformation of interconnected aggregates[33] or to transient cross-links in the polymer due to the presence of the filler.[31,32]

WRC also predict power-law dependence of modulus on loading.

$$E \sim E_f \phi^{(3-c)/(3-d_m)} \tag{10}$$

This relationship, which predicts a power-law exponent between 3.3 and 4.4, is hard to check because, to achieve high enough loadings, the hard aggregates must be broken down to small sizes and uniformly dispersed, which is difficult in normal compounding. High loadings are required to verify the theory, which assumes a connected network. Nevertheless, Klüppel finds that this relationship is obeyed for carbon-black-reinforced rubber where the exponent on ϕ is 3.5, in agreement with eq 10.[34] This relationship has also been verified for powder compacts[35] and aerogels.[36]

3.2. Carbon Nanotube Fillers. 3.2.1. Single-Walled Carbon Nanotubes (SWCNTs). 3.2.1.1. SWCNT Suspensions. The interpretive concepts reviewed for precipitated silica agglomerates and aggregates have been widely used to infer the structure of aggregated quasi-spherical colloidal particles. As a consequence, there is general consensus not only on morphology but also on the chemical and physical processes by which complex, hierarchical structures form from quasi-spherical entities.[34] For low-dimensional systems, such as rods and disks, however, there is no settled wisdom. Lack of consensus is traceable to the limited scattering data extending to low enough *q* to infer large-scale morphology. In addition, experiments are more difficult since filler loadings are typically less than 1 wt %, so scattering is weak. Also, even at this concentration, high aspect ratio objects are doomed to interact with each other, leading to nonworkable viscosities and poor dispersion. In spite of the paucity of data, some important conclusions can be inferred on the basis of small-angle neutron and X-ray scattering (SANS and SAXS) from solutions and composites loaded with single- and multiwalled carbon nanotubes (MWCNTs).

Figure 7c shows combined light scattering and ultra-small-angle X-ray scattering (USAXS) data from a SWCNT/H_2O solution with sodium poly(styrenesulfonate) as a dispersion aid.[37] These data can be interpreted using similar concepts as

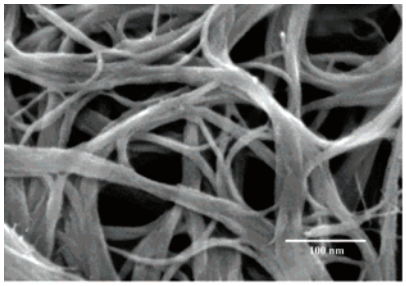

(a)

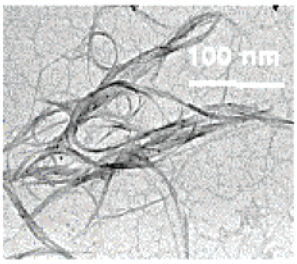

(b)

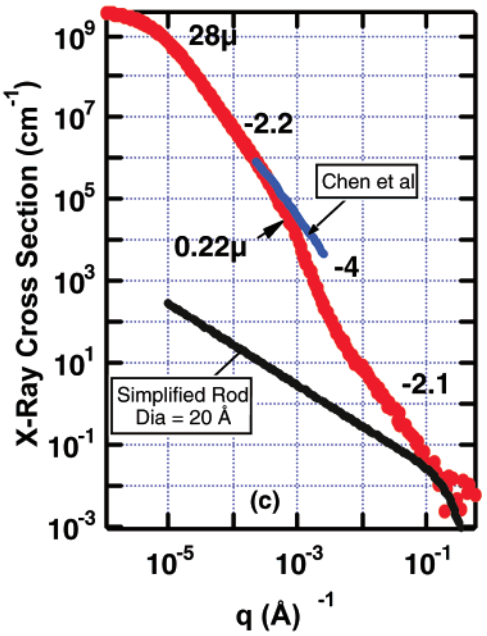

Figure 7. (a) SEM, (b) TEM, and (c) small-angle scattering (SAS) data on single-walled carbon nanotubes. SAS data are from a 0.1% water solution.[37] The SEM and TEM images were taken from dried samples. The X-ray data ($q > 0.0003$ Å^{-1}) are on an absolute scale. The light scattering data ($q < 0.001$ Å^{-1}) were scaled to match the X-ray data. The scale bars in both images are 100 nm. The light scattering data of Chen et al.[39] have been shifted to match small-angle data. The data at $q > 0.1$ Å^{-1} are too noisy to extract information regarding the local carbon structure, which in principle should show up in this region.

developed above for precipitated silica. The most notable feature of the profile is the absence of a power-law scattering with an exponent of -1, the signature of a one-dimensional scatterer. Since the data are on an absolute scale, they can be compared with the expected scattering from a one-dimensional rod. The simplified rod model[38] in Figure 7c matches the data only at the highest q. Over the entire region where a rodlike power-law (slope -1) profile is expected, the measured intensity is orders of magnitude greater than the value calculated assuming isolated SWCNTs. The excess scattering at small q presumably arises because SWCNT clusters are present, not unlike the case for precipitated silica. Clustering leads to larger mass per unit volume and therefore enhanced intensity at small q.

Scanning electron microscopy (SEM) and TEM images (Figure 7a,b) help in the interpretation of these SAS data. The images show that, on length scales above 1000 Å, the dried SWCNT sample is organized into a ropelike network. The mass-fractal character of the SAS data around $q = 3 \times 10^{-5}$ Å^{-1} suggests this network structure persists in solution. Therefore, the predominant product of dispersion is not independent nanotubes but microgel networks tens of microns in radius. These clusters can actually be seen by optical microscopy, although their internal structure cannot be resolved with this technique (Figure 8).[3] It should be noted that scattering is sensitive to the square of the mass, so it is difficult to detect small objects in the presence of large. Undoubtedly, some isolated nanotubes are present.

The transition to a slope of -4 at a length scale of 720 Å in Figure 7c fixes the mean radius of the ropes. This number is substantially larger than the ~250 Å rope radius estimated from the microscopy in Figure 7a. The difference implies the ropes are highly swollen but not completely destroyed during water dispersion. With sufficient mechanical disruption, however, the ropes can be completely obliterated, leaving a slope of ~-2.5 across the entire scattering profile.[39−44] The data of Chen et al. (included in Figure 7c) show no crossover to -4 at high q.[39]

For SWCNTs, a second mass-fractal, power-law region is observed at $q > 5 \times 10^{-3}$ Å^{-1} (Figure 7c). This behavior implies

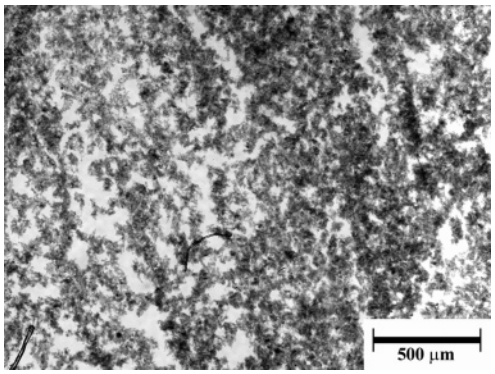

Figure 8. Optical microscopy of SWCNTs in Jeffamine D400.[3] Large-scale SWCNT clusters are evident.

considerable disorder inside the swollen ropes. In solution, therefore, the ropes are not organized structures; instead, the ropes exist as disorganized network structures similar to the TEM image in Figure 7b. A more realistic cartoon of SWCNT morphology in solution is shown in Figure 9 as suggested by Brown et al.[3] This hierarchical morphology shows disorder on two length scales but retains some semblance of ropelike character.

Instances have been reported in the literature where power-law scattering with exponents of -1 has been observed in SWCNT suspensions. Schaefer et al. observed such behavior when SWCNTs are suspended using a poor dispersant and sonicated until most of the carbon flocculates.[37] The remnant suspended carbon has rodlike character—either isolated SWCNTs or rodlike bundles. Power-law exponents of -1 have also been observed by neutron scattering in SWCNT solutions of micelle-forming surfactants.[44,45] In this case, large background subtraction is necessary because of the scattering from the surfactant micelles. This subtraction is compromised, however, since the organization of the surfactant is likely perturbed by the nanotubes.

Figure 10 shows background-subtracted neutron scattering from a 0.1% SWCNT solution suspended in D_2O containing

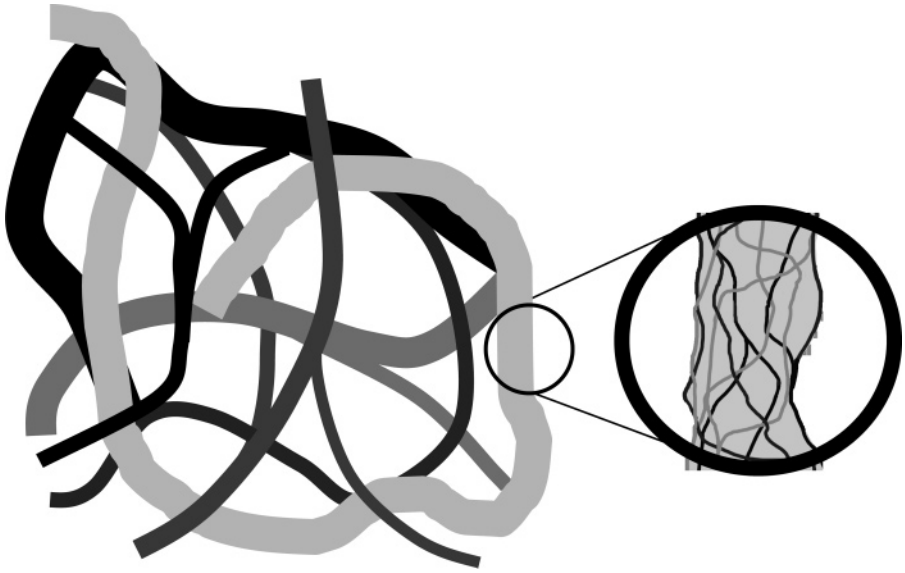

Figure 9. Schematic representation of a suspension of SWCNTs showing a disordered network on two length scales.[3] The pattern on the left represents bundles or ropes of SWCNTs. Within the solvent-swollen bundles, the individual SWCNTs also form a disordered network structure.

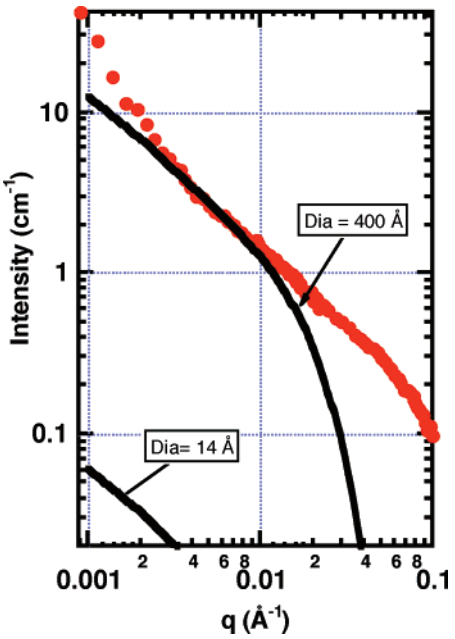

Figure 10. SANS data[45] for SWCNTs suspended in D_2O are compared with expected scattering from 14 and 200 Å diameter rods. Neither model fits the data, so the region of power-law behavior with slope of −1 is probably not related to rodlike morphology of the isolated SWCNTs.

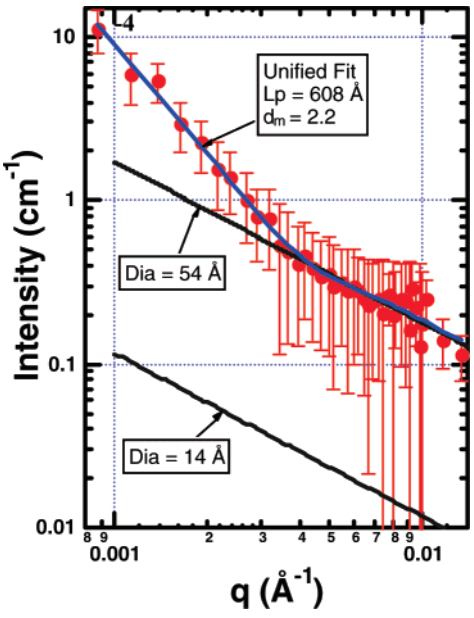

Figure 11. Background subtracted SANS data for SWCNTs suspended in $D_{0.34}H_{1.66}O$ using 0.2 wt % NaDDBS as a dispersion aid. Data are from Zhou et al.[44] The SWCNT concentration is 0.02 wt %. The data are compared to scattering from a 14 and 54 Å diameter carbon rods of density = 1.4 g/cm^3. In the latter case, a unified fit is used to find the crossover to fractal behavior at small q. Based on the unified fit the effective aspect ratio is α = 608 Å/27 Å = 24.

0.5 wt % surfactant.[45] These data are compared with the expected scattering from a 14 Å diameter carbon rod with a density of 1.4 g/cm^3. Comparing the data and the isolated-rod calculation, the observed intensity is more than 2 orders of magnitude too large to be attributed to isolated SWCNTs. In order to match the intensity, a rod diameter of 200 Å must be assumed, but in that case the high-q data cannot be fit (Figure 10). Yurekli et al. suggest such data can be interpreted assuming surfactant decoration of the nanotube walls.[46] These authors also note problems associated with such an interpretation, one of which is the inability to fit the entire curve, as illustrated by the 200 Å rod calculation in Figure 10.

To avoid the compromises caused by the presence of surfactant, Zhou et al. used a mixture of D_2O and H_2O to contrast match the sodium docecylbenzenesulfonate (NaDDBS) surfactant (Figure 11).[5] This method minimizes the masking of the SWCNT scattering by the surfactant scattering, but the presence of H_2O increases the background due to incoherent scattering from hydrogen atoms. Large subtraction errors make it difficult to establish definitively the presence of a −1 slope necessary to confirm rodlike morphology. Since the data are on an absolute scale, however, we can compare the observed intensity in the ostensibly power-law regime with that expected from isolated linear nanotubes. Figure 11 includes the prediction for 14 and 54 Å diameter carbon rods. The fact that the latter matches the data in the large-q region means there is some side-by-side aggregation of nominally 14 Å diameter isolated SWCNTs. At low q, the data follow a slope of −2.2, consistent with large-scale fractal networking discussed above. The crossover point is the persistence length from which an effective aspect ratio of α = 608 Å/27 Å = 24 is calculated (note that L_p

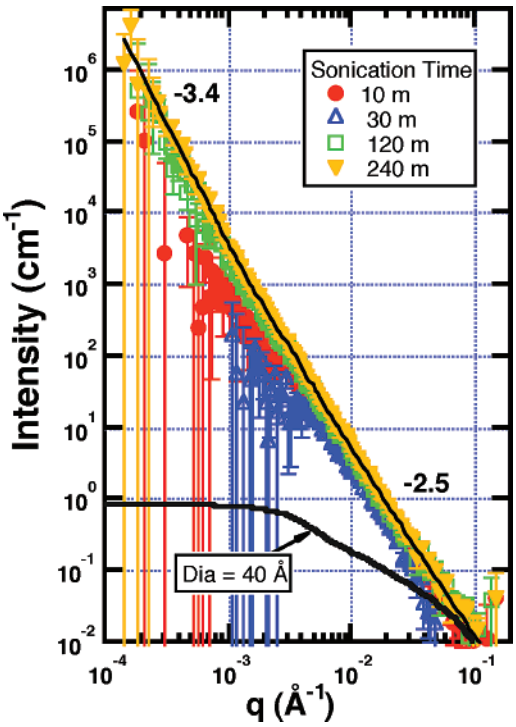

Figure 12. Background-subtracted USAXS data for Epon 828 cured with SWCNT-loaded Jeffamine D-2000.[3] Sonication time refers to the Jeffamine D-2000−SWCNT precursor suspension. The carbon loading is 0.1 wt %. The data are compared to scattering expected from a 40 Å diameter, 1400 Å long, isolated carbon rod. The data imply extensive clustering on all length scales, which increases with sonication.

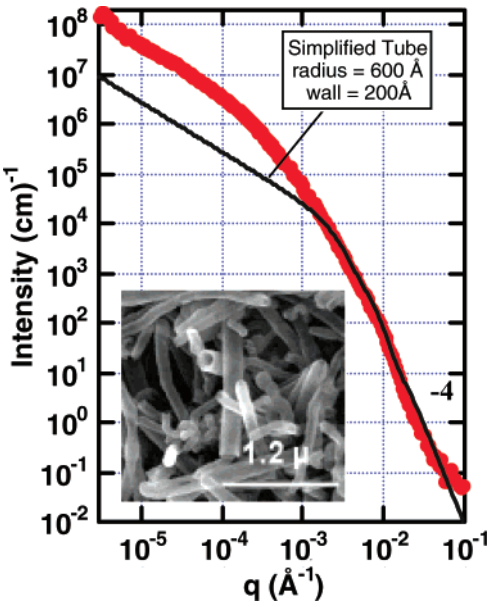

Figure 13. Combined light and X-ray scattering from a 0.5 wt % water suspension of vapor-grown nanofibers.[40] The solid line is a simplified tube calculation with dimensions comparable to that in the TEM inset. The data are plotted as X-ray scattering cross section per unit volume. The light scattering data (q < 0.001 Å^{-1}) were scaled to match the X-ray data. To account for the broad crossover between the high- and low-q power-laws, it is necessary to assume tube radii between 600 and 5500 Å. This latter number is much larger than any individual tubes, which implies side-by-side aggregation. The effective aspect ratio cannot be extracted from these data because the persistence length is larger than $1/q_{minimum}$.

is a half-length). These data are therefore consistent with SWCNT ropes with a rather short persistence length. To our knowledge, there are no literature values to which this value of the effective persistence length can be compared.

3.2.1.2. SWCNT Composites: Thermosets. SWCNTs are weak scatterers that are very difficult to disperse in polymers at loadings above 0.1 wt %. At this loading, it would be difficult if not impossible to observe X-ray or neutron scattering from isolated SWCNTs. As a result, there is little morphological data on SWCNTS in engineering composites. The only SWCNT−thermoset USAXS data we know of is shown in Figure 12. Brown et al.[3] prepared these composites by dispersing the SWCNTs in the curing agent (Jeffamine D-2000) before mixing with the epoxy resin. These authors find that SWCNTs do not disperse in the epoxy itself.

Figure 12 shows the evolution of the scattering profile as a function of sonication time in the curing agent. Comparison with the expected scattering from isolated 40 Å diameter carbon rods shows that the observed scattering far exceeds that expected from well-dispersed SWCNTs. In fact, the only reason scattering is observed above background is that the SWCNTs are aggregated on all observable length scales. Since the scattering intensity increases with sonication time, the concentration of micron-sized aggregates increases with time. This increase could be attributed to aggregation of smaller clusters or dispersion of agglomerates so large as to exceed the resolution of USAXS. On the basis of visual observation, the latter is probably the case. Since there is no signature of rodlike scattering in these data and no distinct Guinier crossovers, it is impossible to associate any length scales with the dispersed carbon.

3.2.2. Multiwalled Carbon Nanotubes and Nanofibers. Carbon nanotubes come in a variety of wall structures including single-walled, double-walled (DWCNT), concentric multiwalled, and more complex multiwalled structures such as stacked cones. MWCNT varieties are much larger and stiffer than SWCNTs. Figure 13 shows a microscopy image as well as combined light scattering and USAXS data for a water suspension of vapor-grown nanofibers (PR-19-PS from Applied Sciences Inc., Cedarville, OH).[40] These fibers normally contain a few concentric cylinders or nested truncated cones.[47] Typically the cores are open and presumably filled with solvent. The data in Figure 13 show power-law scattering at both large and small q. The power-law slope of −4 at high q is indicative of smooth tube walls. The slope of −1.09 at small q is close to that expected for a stiff one-dimensional structure.

For comparison, Figure 13 includes a simplified form factor of a rigid tube of radius 600 Å and a wall thickness of 200 Å, approximately the dimensions seen in the SEM inset. The simplified tube form factor[48] is similar to the simplified rod form factor[38] used in Figures 7, 10, 11, and 12 in that it matches the exact tube form factor but suppresses the oscillations observed in the exact calculation. Such oscillations are seen only with highly monodisperse samples. The simplified tube form factor fits the data in Figure 13 at intermediate q, where the scattering is controlled by the wall thickness; it fails at low q, however, because of the broad distribution of tube radii. To account for the broad crossover between the high and low-q power-laws, it is necessary to assume tube radii between 600 and 5500 Å. This latter number is much larger than any individual tubes, which implies side-by-side aggregation.

The suspension in Figure 13 was prepared using sodium poly(styrenesulfonate) as a dispersion aid. In the absence of the dispersion aid, the fibers remain aggregated in 20 μm clusters, and no slope of −1 is observed.[47] These unmodified tubes precipitate rapidly. If the tubes are surface-modified by acid treatment to make them more hydrophilic, then smaller, more persistent clusters are observed following dispersion by sonication. After about 50 h, however, the cluster size approaches

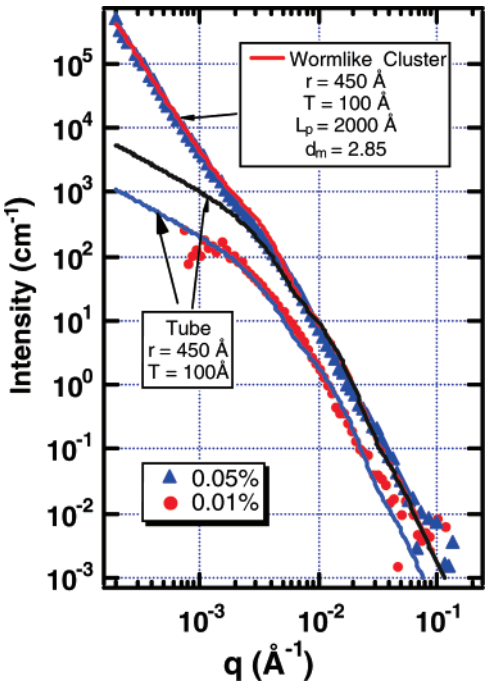

Figure 14. USAXS data for a bismaleimide thermoset loaded with multiwalled carbon nanotubes.[48] The lines are fits to infinitely long, isolated tubes and a wormlike tube cluster, assuming a carbon wall density of 1.9 g/cm^3. T is the wall thickness, and r is the outer radius. A background of pure resin has been subtracted. The lines represent calculated scattering for isolated and aggregated tubes. The fact that the scattering is reasonably modeled on an absolute scale gives confidence that the scattering is actually due to carbon. The effective aspect ratio is 4.4. Since this ratio depends on the nature of the nanotubes (wall thickness, diameter, wall morphology) as well as processing, it is not surprising that the value depends on the specific system under study. What is surprising is that the effective aspect ratio is less than 10 for all the systems analyzed here.

20 μm, and the modified tubes also precipitate. Surface modification slows agglomeration, but eventually the fate of surface-modified tubes is the same as that of pristine tubes. It is very difficult to suppress agglomeration by surface modification. Surface modification may be helpful, but it must be combined with other strategies such as the use of shorter nanotubes.

3.2.2.1. CNT-Filled Composites: Thermosets. Because of the difficulty in gathering light scattering data on solid samples, direct evidence regarding the large-scale morphology of nanotubes in solid matrices is sparse. Being cognizant of information reviewed above regarding suspensions, however, it is possible to draw some important conclusions about composite morphology from USAXS. It is not surprising that nanotube-reinforced composites show complex hierarchical morphology.[3,38,48] We will review composites based on thermosets, thermoplastics, and thermoplastic elastomers.

Consider first the USAXS profiles (Figure 14) for catalytically grown MWCNTs (MER Corp., Tucson, AZ) in a bismaleimide resin.[48] To achieve uniform dispersion, the functionalized nanotubes were subjected to bath sonication and high-shear mixing in the two-part resin prior thermal curing. Since the data are on an absolute scale, they can be compared to the expected scattering from isolated tubes. The 0.01 wt % sample and the high-q region of the 0.05 wt % sample nicely match the simplified tube form factor (STFF)[48] assuming a tube outer radius, r, of 450 Å and a wall thickness, T, of 100 Å, both of which are reasonable on the basis of SEM images. At higher loading, however, the STFF fails to account for the excess scattering at low q. It should be pointed out the low-q region in the lightly loaded sample is not available due to large background subtraction errors at very small scattering angles. Therefore, one cannot definitively say that the 0.01 wt % sample is unaggregated. The excess scattering at small angles for the 0.05% sample, on the other hand, is consistent with a network entangled, semiflexible nanotubes.

To model the scattering from hierarchical structures, we use a wormlike cluster model.[48] That is, we assume isolated tubes for distances less than a persistence length, L_p. At distances larger than the L_p, a mass-fractal network morphology with fractal dimension, d_m, is assumed. A cartoon of an isolated "wormlike tube cluster" is shown in Figure 15a. If such clusters are part of a percolated network, fractal correlations would exist up to a correlation range beyond which the carbon distribution would be uniform, similar to the situation in a semidilute polymer solution. This cutoff length scale is larger than the resolution limit of USAXS ($\sim$1 μm).

Thinking about reinforcement in light of Figure 15a evokes the WRC model of reinforcement by fractal objects. Applying the analysis of Figure 4 leads to the conclusion that clusters larger than a typical tube diameter offer minimal reinforcing potential in hard materials. In other words, the flexibility and clustered nature of the tubes eliminate the potentially beneficial effects of high-aspect-ratio carbon nanotubes. In this system, the processes of functionalization, sonication, and high shear mixing, which are necessary to achieve dispersion, have destroyed the high aspect ratio of the native carbon nanotubes. Presumably the tubes are broken, kinked, and elastically deformed by the processing. This point is further developed below.

3.2.2.2. CNT-Filled Composites: Thermoplastics. Figure 16 shows USAXS data of Zhao et al. for 0.5 wt % MWCNTs in melt-processed thermoplastic polyamide 6 (PA6).[38] These data are for unfunctionalized nanotubes, but the data are the same for functionalized counterparts. The data are consistent with a wormlike cluster model assuming a persistence length of 800 Å, a rod radius of 152 Å, and a cluster fractal dimension of $d_m = 1.6$. No isolated rod model can fit the data. Small-radius isolated rods can fit the high-q region, but not the low q. Thicker rods do better at low q but misrepresent the high-q portion. This rather low value of d_m compared to Figure 14 implies a more open cluster.

On the basis of the very short persistence length found from USAXS, one would not expect significant reinforcement of PA6, which is the case (Figure 17). As was observed for thermosets, clusters are poor reinforcing agents, so reinforcement depends on the short rodlike segments that make up the clusters. As will be explained below, however, short rods are also poor reinforcing agents.

There is little difference in the tensile data for PA6 and PA6 with either functionalized or unfunctionalized nanotubes (Figure 17). When clusters are present, functionalization has minimal impact on modulus enhancement. It should be pointed out, however, that other groups find modulus enhancement up to a factor of 2 at 2.0 wt % loading. The absolute values, however, are much lower than the common PA6 resins.[49]

3.2.2.3. CNT-Filled Composites: Thermoplastic Elastomers. The situation for elastomers is similar to that found in thermosets and thermoplastics. Figure 18 shows data for Irogran (PS455-203, formally Morthane, Huntsman Polyurethanes) thermoplastic elastomer reinforced with ASI PR19-HT nanofibers. These samples were prepared by sonication of a THF−polyurethane−CNT mixture followed by casting and evapora-

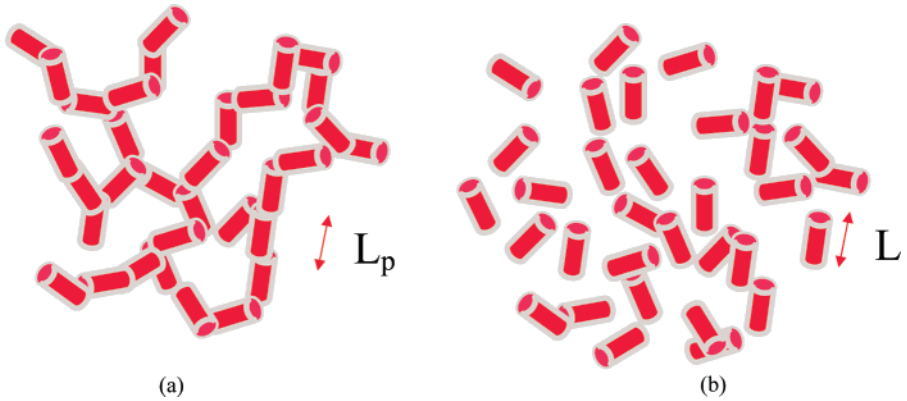

Figure 15. (a) Schematic representation of a branched wormlike cluster with persistence length L_p. (b) Short-fiber mechanical equivalent of the wormlike cluster. The idea is that, to some approximation, the filler behaves mechanically as a disconnected bunch of short rods whose aspect ratio is much less than the aspect ratio of the native, undistorted filler. Since all connectivity is neglected, this model is bound to underestimate the actual modulus enhancement factor, but for hard materials predictions are within a factor of 4 of observations.

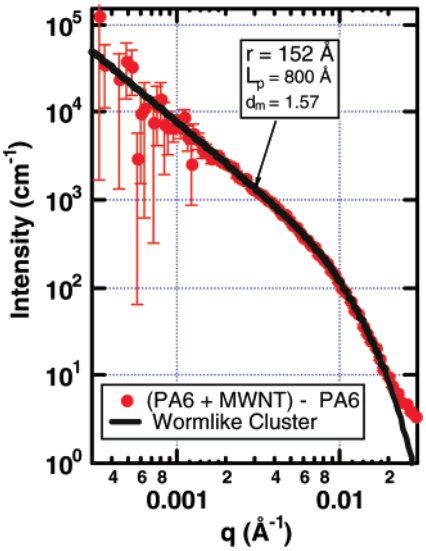

Figure 16. USAXS data for Polyamide 6−MWCNT composite.[38] The data are compared to a wormlike cluster model with a persistence length of 800 Å. The loading is 0.5 wt %. The effective aspect ratio is 5.3.

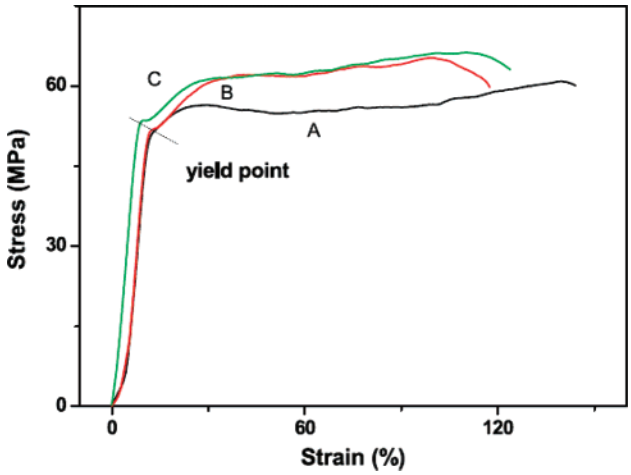

Figure 17. Tensile stress−strain data for PA6−MWCNT composites.[38] A = PA6, B = PA6 + MWCNT, and C = PA6 + MWCNT−COOH (functionalized). The loading is 0.5 wt %. Apart from what appears to be an offset at low strain, these data are very similar in the elastic regime. We assume the small strain slopes are not reliable since the authors were focused on ultimate properties.

tion of solvent. The tube-cluster parameters are listed in the figure. The persistence length of 5000 Å is somewhat longer than that observed for thermosets and thermoplastics. The difference is probably due to the fact that the elastomer composites were cast from solution without high-shear mixing.

3.2.3. Mechanical Properties of CNT-Filled Composites. Regardless of the matrix (thermoplastic, thermoset, elastomer), USAXS data imply large-scale morphology as in Figure 15a. In the context of mechanical models of composites, such an object maps on to a short-fiber equivalent as shown in Figure 15b. That is, flexibility and clustering reduce the effective aspect ratio, α, of the native carbon fiber. The reduced aspect ratio has dramatic affects on mechanical properties because short-fiber composites have reduced moduli compared to long-fiber composites.

Ideal long-fiber composites should follow the rule of mixtures. If E_c is the modulus of the composite, E_m the modulus of the matrix, and E_f the modulus of the fiber, the modulus enhancement, E_δ, is

$$E_\delta = \frac{E_c}{E_m} = \left(\frac{E_f}{E_m}\right)\phi + (1 - \phi) \qquad (11)$$

where ϕ is the volume fraction fiber.

Equation 11 is simply derived assuming equivalent strain on the matrix and fibers. The fibers are also assumed to span the sample ($\alpha \gg 1$) and to be aligned with the applied stress. Note the Smallwood result (eq 6) would obtain in the opposite limit ($\alpha = 1$) corresponding to spherical particles. Between these two limits lies the "short-fiber" regime.

Modeling of short-fiber composites is quite complex. Although more than one approach to the short fiber problem can be found in the literature,[50] all lead to the conclusion that short fibers show drastically reduced reinforcement compared to long fibers. Two factors reduce reinforcement: the finite length of the fibers and random orientation. The orientation factor reduces the effective modulus by a factor, C_a, of 0.2 for randomly oriented fibers (see below). For most applications of nanocomposites, this sacrifice is acceptable because alignment of fibers leads to degradation of transverse properties. The real problem comes from the length factor, which drops as α decreases.

The calculation of the length factor is more complicated. Fukada and Kawata[51] calculate this factor for isolated fibers in the isostrain approximation for which eq 11 is the long-fiber limit. Halpin and Tsai[52] include multifiber interactions and find that many solutions reduce to the same form.[53] Mori and Tanaka treat the fiber as ellipsoids of revolution.[54−56] Any of these models could be used to illustrate the impact of reduced fiber

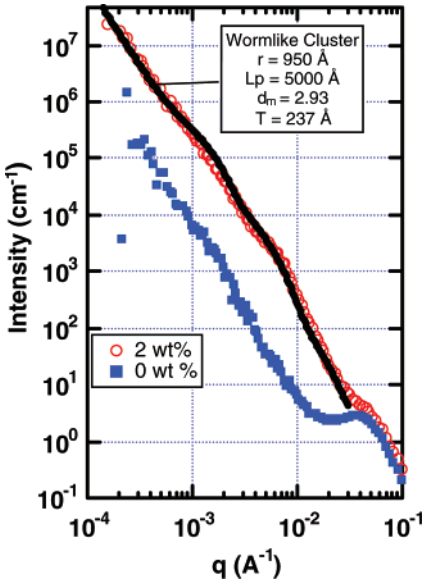

Figure 18. USAXS data for polyurethane thermoplastic elastomer loaded with vapor-grown carbon nanofibers. The line is a wormlike tube cluster model assuming a tube−wall carbon density of 2.1 g/cm^3 and a matrix composition of $C_{36.4}H_{36.8}O_{9.8}N_2$ and a density of 1.11 g/cm.

length. We will examine the Halpin−Tsai model since it reduces simply at interesting limits. For fully aligned fibers, the "Halpin−Tsai" equation is

$$E_\delta = \frac{1 + 2\alpha\eta\phi}{1 - \eta\phi}$$

$$\eta = \frac{E_f/E_m - 1}{E_f/E_m - 2\alpha} \tag{12}$$

In the dilute, stiff fiber limit ($\phi \ll 1$ and $E_f/E_m \gg 1$) this equation reduces to

$$E_\delta = 1 + 2\alpha\left(\frac{E_f/E_m}{E_f/E_m - 2\alpha}\right)\phi \tag{13}$$

In the long fiber limit ($2\alpha \gg E_f/E_m$) eq 12 reduces to the rule of mixtures. In the short fiber limit ($2\alpha \ll E_f/E_m$) eq 13 becomes independent of fiber elastic properties

$$E_\delta = 1 + 2\alpha\phi \tag{14}$$

which, for $\alpha = 1$, is close to the Smallwood calculation (eq 6) for rigid spheres. If the fibers are not aligned, the angular factor discussed above must be included, giving

$$E_\delta = 1 + 2\alpha C_a\phi \tag{15}$$

Fukada and Kawata[51] find that $C_a = 0.2$ for randomly oriented fibers.

Using the parameters in Figure 14 and identifying L_p as the effective fiber length, $\alpha = 4.4$ so $E_\delta = 1 + 1.8\phi$, which is to be compared to the rule-of-mixtures result of $E_\delta = 1 + E_f/E_m\phi \cong 1 + 1000\phi$. Whereas the rule of mixtures predicts a 5-fold increase in modulus at 1 wt % loading, the short-fiber calculation predicts negligible modulus enhancement. The modulus data in the literature seem to cover the range between these two calculations. For the SWCNT data in Figure 11, $\alpha = 24$ so the prediction, based on the solution morphology, is $E_\delta = 1 + 9.6\phi$.

Gojny et al.[57] studied a variety of nanotubes in an epoxy matrix. Figure 19 shows their data for SWCNTs, DWCNTs, and MWCNTs. The tensile data (Figure 19a) are nearly identical at small strain, suggesting that there is little change in elastic properties with loading. Gojny et al.'s analysis of these data, however, shows a modest dependence of modulus on loading (Figure 19b). The line in the figure is $E_\delta = 1 + 30\phi$, from which an aspect ratio of 75 ± 35 is calculated using eq 15. This number is larger than the persistence length determined in similar systems by USAXS but is substantially smaller than that of pristine tubes.

The only case where both scattering data and modulus data are available on the same sample is for the thermoplastic polyamide 6 in Figure 16, which shows a very short persistence length and negligible modulus enhancement (Figure 17). This result agrees with the predictions of eq 15.

Equation 15 is independent of the elastic properties of both the fiber and the matrix, so it predicts minimal reinforcement of elastomers as well as thermosets. The evidence, however, is that nanotubes are more effective in reinforcement of elastomers than thermosets. Koerner et al., for example, measured the modulus of the same polyurethane−nanotube thermoplastic elastomer (Figure 20). Based on eq 15 and the parameters in Figure 18, $E_\delta = 1 + 2.1\phi$. The data in Figure 20, however, give $E_\delta = 1 + 109\phi$. If the aspect ratio is calculated from eq 15, the result is $\alpha = 270$, which is much larger than $\alpha = 5.3$ from the data in Figure 18. Apparently the short-fiber model substantially underestimates the reinforcement effect in soft materials.

The superior performance of nanotubes in elastomers as compared to thermosets is consistent with the WRC model. In the WRC model, elastic energy is stored in the compressive strain of the filler aggregate, an effect that is not included in the Halpin−Tsai equations. As discussed with reference to Figure 4, fractal aggregates are expected to be more efficient in the reinforcement of soft materials compared to hard materials. This prediction seems to be borne out by the data, although it must be acknowledged that there is no consensus on this issue among workers in the field.

3.3. Layered Silicates. 3.3.1. Layered Silicate Suspensions. Exfoliated layered silicates (clays) are two-dimensional colloidal fillers that have been widely studied as reinforcing agents for polymers.[1,58] As was observed for CNTs, the claims vary widely regarding the degree of reinforcement attributable to these sheetlike colloids. Although numerous imaging and scattering/diffraction studies of the morphology of dispersed layered silicates exist, troubling discrepancies remain in the interpretation of these data. Published TEM images typically show platelike entities that are flat (i.e., linear when viewed in projection) over 0.1 μm length scales, whereas SAS profiles seldom show power-law exponents of −2, the signature of isolated, platelike objects. By examining scattering data in solution and in polymer matrices, we will show that layered silicates display large-scale disorder similar to that observed for CNTs and precipitated silica. Similar concepts apply—sheetlike morphology is found only on short length scales. On larger scales, fractal correlations exist, which are consistent with crumpling, aggregation, and/or networking.

The extent of dispersion of layered silicates in polymer nanocomposites is reflected in both SAXS and USAXS. In the SAXS regime, diffraction peaks reveal the layer spacing and layer perfection of the multilayer stacks (tactoids). As the tactoids exfoliate and disperse, the layer peaks shift to smaller q and broaden.[59−61] USAXS can then be employed to probe at larger length scales and reveal the size and perfection of the individual platelets as well as the morphology of tactoids. Ho,

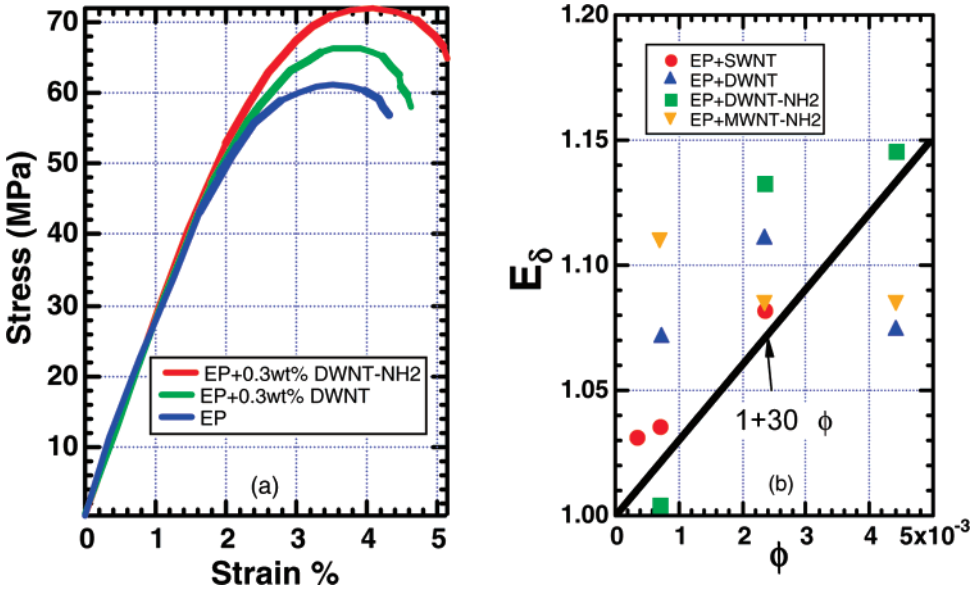

Figure 19. Tensile data for DGEBA-based epoxy loaded with SWCNTs, DWCNTs, and MWCNTs, both pristine and amine-functionalized.[57] Although the tensile data are nearly identical at small strain, the collection of data do show a modest dependence of the modulus enhancement on loading in (b).

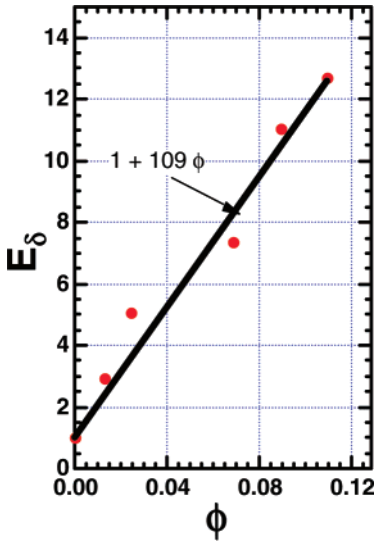

Figure 20. Koerner's et al. modulus data[74] for the polyurethane elastomer system in Figure 18.

Briber, and Glinka[60] calculate the scattered intensity for a distribution of multiple-layer tactoids, whereas Vaia, Liu, and Koerner[59] treat a mixture of monodisperse multilayer tactoids and fully dispersed individual sheets. In both cases, the large-scale morphology is platelike. In both cases, the authors note deviations of the measured data at small q from the predictions of the platelet-based models.

Figure 21 shows the measured USAXS data for sodium montmorillonite (NaMMT) in water. The line represents the expected scattering from an infinite disk of thickness $H = 9.8$ Å at 0.1 wt %. A simplified disk form factor (similar to the simplified rod and tube form factors described previously) was used to calculate the lines in Figure 21a.[62] The electron density was calculated assuming a NaMMT chemical formula of $Na_{0.65}Al_4Si_8O_{22}H_{20}$ and a density of 2.85 g/cm^3. The excellent fit at $q > 0.01$ Å^{-1} confirms full exfoliation of the clay platelets. The slope of -2 and absolute intensity at large q are consistent with scattering from isolated two-dimensional platelets. The absence, within error, of a layer diffraction peak at high q is also consistent with full exfoliation.

For $q < 0.01$ Å^{-1}, the data lie above the rigid-disk form factor and approach a power law with an exponent of about -2.7 at small q. This deviation evokes the same interpretative concepts as applied above to similar deviations for CNTs. Apparently, large-scale fractal like disorder is present at large length scales. Because of the excellent agreement with the simplified disk form factor at large q, we argue that the low-q scattering must be due to a fractal arrangement of the sheetlike units (facets), giving rise to the high-q scattering. A crumpled or faceted sheet is an example of such morphology. To model small-q scattering, we consider a fractal aggregate in which the local structure is modeled as platelike facets with a thickness, H, and a persistence length (facet radius), R_p.[62] The long-range fractal correlations give rise to power-law scattering of mass fractal form up to a cutoff at a size, ξ, of the overall size of aggregate.[63] A schematic of this structure is shown in the inset of Figure 21b.

3.3.2. Layered Silicate Composites. Faceted sheet morphology also exists in polymer composites. Figure 22 compares the data for fully exfoliated MMT in water to data for organically modified MMT melt-compounded in polyamide-66 (PA66).[62] On the basis of TEM data (inset), the filler seems to be dispersed as sheets. The USAXS data, however, suggest an alternative description. Both samples are qualitatively similar to NaMMT in water at low q, except that the low-q power-law implies a larger fractal dimension ($d_m = 2.9$) corresponding to more compact crumpling. This value is very close to 3, corresponding to a globular nonfractal cluster. The samples also differ at large q in that the "exfoliated" sample crosses over to a slope of about -2, whereas the "partially exfoliated" sample shows no crossover. Disorder persists down to dimensions comparable to the sheet thickness.

The issue of why TEM images show streaks that seem to be edge views of large rigid plates is yet to be resolved. Hopefully this discussion will encourage microscopists to reinvestigate the meaning of clay images and accept simple descriptions with a degree of caution. The fact is images like the inset in Figure 22 show fuzzy contrast regions that one would expect for disordered fractal objects. Such regions exceed the area occupied by the linear objects to which the eye is attracted. Also, imaging always involves a trade off of contrast and resolution,[64] which may

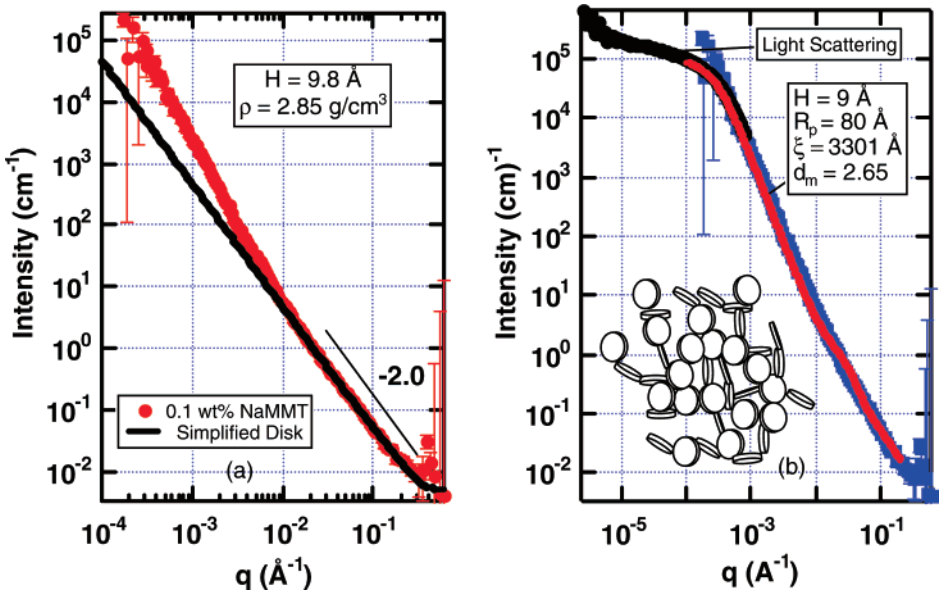

Figure 21. (a) USAXS data for sodium montmorillonite (NaMMT) clay in aqueous solution. The line in (a) is a simplified disk form factor.[62] (b) Light and USAXS data for 0.1 wt % NaMMT in water compared to the faceted-sheet model, a schematic of which is shown in the inset.[75] The very small facet size, R_p, indicates the sheets are flat only over a limited distance. On large scales the sheets are probably crumpled. In (b) the light scattering data were scaled to match the USAXS data. H is the disk thickness, ξ is the overall cluster size, and d_m is the mass-fractal dimension. The effective aspect ratio is $\alpha = 80$ Å/4.5 Å $= 18$.

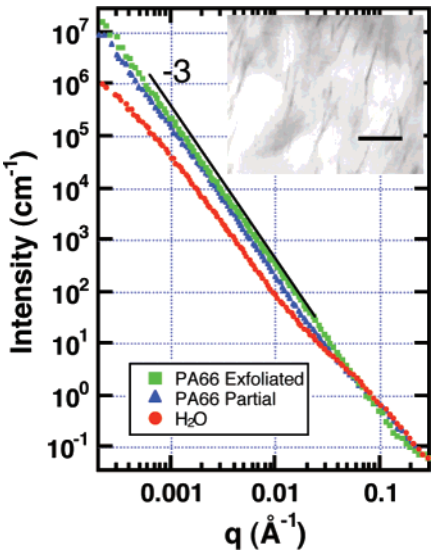

Figure 22. Comparison of exfoliated and partially exfoliated organically modified MMT melt compounded in PA-66.[62] The inset is a TEM of the exfoliated sample. The bar is 1000 Å.

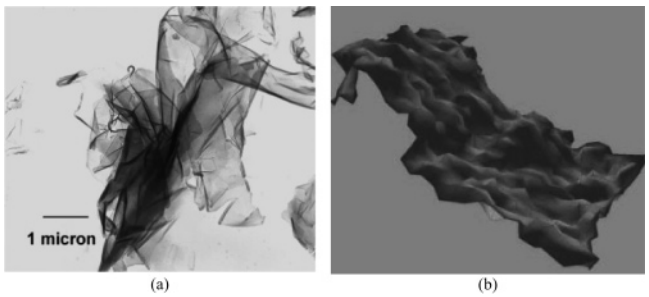

Figure 23. (a) TEM of a crumpled layered silicate (measured by Hartmut Fischer, see acknowledgment) and (b) simulation of an elastic membrane.[65]

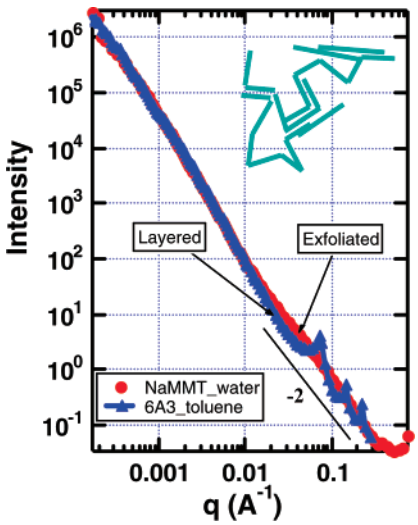

Figure 24. Comparison of an exfoliated sodium montmorillonite clay in water with its layered, organically modified counterpart in toluene. The layered data have been shifted to overlap the water-solution data. The inset shows, in projection, how a semiflexible sheet could be ordered at small scales and disordered at large scales.

obscure disordered structures, particularly when the operator is looking for platelets.

Some evidence of sheet flexibility exists from both TEM and simulations. Figure 23 shows a TEM of a crumpled clay sheet and a simulation of a tethered (i.e., elastic) membrane.[65] The TEM illustrates crumpling occurs in single clay layers. The simulation shows that crumples are thermally activated in a thin elastic sheet. Furthermore, long-range disorder is also found in clay dispersions that show significant layering. For example, Figure 24 shows USAXS data from organically modified MMT in toluene compared to NaMMT in water. The former shows layer diffraction peaks at large q indicative of significant layering. At small q, however, the scattering from the layered sample is identical to the fully dispersed water sample. On the basis of the interpretation of the water data, layering occurs only over short distances. The inset in Figure 24 shows a cartoon to illustrate how a sheetlike object could be ordered at short scales and disordered on large scales. The origin of large-scale disorder in layered silicates is the same as observed for CNTs. First of all, silicates are not as rigid as the cartoons suggest. Additionally,

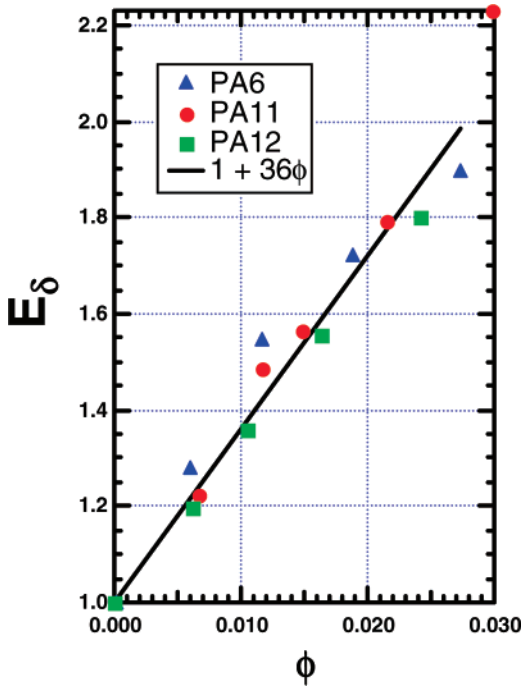

Figure 25. Modulus vs loading for three polyamides. The line is a fit to the combined data. Data are from Fornes and Paul.[70] The enhancement factor of 36 is twice that calculated from the effective aspect ratio from the scattering data (Figure 21) and 1/30 of that calculated from the aspect ratio of 1000 estimated from the TEM inset in Figure 22.

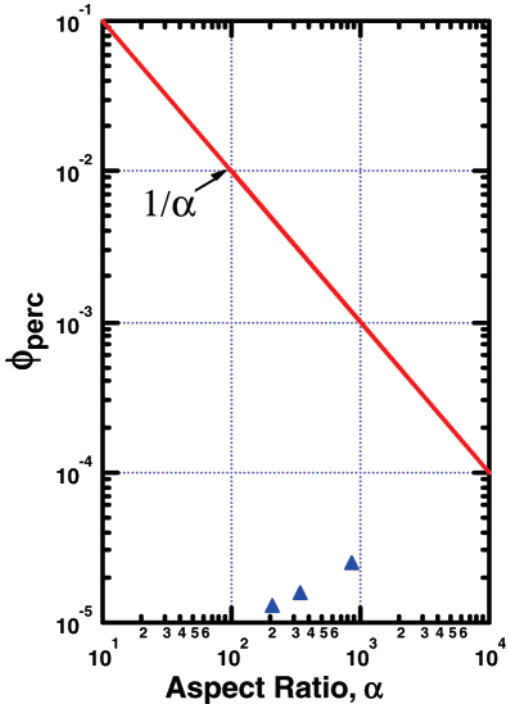

Figure 26. Percolation threshold measured by Martin et al. compared to ideal percolation of rods of aspect ratio α.[71]

layered silicates are exfoliated and dispersed by chemical modification, sonication, and high-shear mixing, just as is the case for carbon nanotubes. These processes lead to defects, tears, crumpling, and even entanglement of sheets.

3.3.3. Mechanical Properties of Layered Silicate-Filled Nanocomposites. According to the Mori−Tanaka theory,[54,55] aligned platelike objects intrinsically reinforce less than aligned fibers,[56,66] so in the absence of disorder, modulus enhancement in clay nanocomposites would theoretically be less than that of carbon nanotubes. Angular averaging, however, has less impact on platelets than on fibers, so randomly aligned platelets are ultimately more effective than randomly aligned fibers in terms of modulus enhancement.[56]

The impact of large-scale disorder on reinforcement by platelets is very similar to that for fibers. The effective size of the reinforcing element is the facet size, R_p, which is an order of magnitude smaller than the size of the native silicate sheet. As in the case of fibers, the effective aspect ratio, α, is reduced from that of an isolated, flat, rigid platelet. For clays, the reduced aspect ratio has the same effect as observed in eq 15—a reduction of the modulus enhancement compared to the rule of mixtures. In fact, eqs 12−15 are widely used to interpret the elastic properties of layered silicate nanocomposites.[67−69] The main difference is the angular factor for clays becomes $C_a \cong 0.5$ as compared to 0.2 for fibers.[56] For platelets, eq 15 is thus

$$E_\delta = 1 + 2\alpha C_a \phi \cong 1 + \alpha\phi \qquad (16)$$

Extracting $\alpha = 18$ from Figure 21b gives $E_\delta = 1 + 18\phi$.

Fornes and Paul[70] studied a series of polyamide−layered-silicate composites. Their data are shown in Figure 25 along with a fit to eq 16 with α as a parameter. The data follow $E_\delta = 1 + 36\phi$, so $\alpha = 36$. The situation is very similar to that found above for nanotubes. The aspect ratio calculated from scattering leads to an underestimate of the mechanical properties. Underestimation is reasonable on the basis of the fact that connectivity between the randomly oriented facets is neglected, and each facet is treated as independent. In addition, the Halpin−Tsai approximation in eqs 15 and 16 assumes that no elastic energy is stored in the filler deformations. Although the idea that disorder reduces modulus enhancement seems to be correct, the "small-disk" approximation, like the short-fiber approximation, is too drastic to predict quantitatively the degree of reduction.

It must be emphasized that we have restricted our attention to elastic properties because elastic properties are least sensitive to defects. Ultimate strength and fracture toughness are probably not as seriously compromised by nonideal filler morphology. Some properties may actually be improved by clustering. We will illustrate this fact by considering electrical percolation, the formation of an electrically conductive path across a macroscopic sample. In this case poor dispersion may be an advantage.

4. Electrical Properties

Figure 26 shows the electrical percolation threshold measured by Martin et al.[71] for CVD-grown MWCNTs in epoxy compared to that predicted for isolated tubes with aspect ratio α. The measured threshold is 2 orders of magnitude below that expected for well-dispersed tubes, for which the percolation volume fraction $\phi_{perc} \cong 1/\alpha$.[72] This reduction of threshold can be attributed to clustering of tubes into fractal clusters. This surprising result obtains because the peripheral density of a fractal cluster approaches zero as the cluster size approaches infinity. As a result, connectivity can be maintained across a cluster even though the volume fraction within the cluster is substantially below the percolation threshold of the fully dispersed subunits. This situation is quite different from compact or globular aggregates, which would percolate at volume fractions larger than that of the fully dispersed subunits.

The reduction of the percolation threshold due to fractal clustering can be estimated by a simple scaling argument, which goes as follows. If N_{cl} is the number of rods in a cluster, the size of the cluster is roughly

$$R_{cl} = L_{eff} N_{cl}^{1/d_m} \tag{17}$$

where L_{eff} is the effective length of the rodlike subunits (persistence length) and d_m is the mass fractal dimension of the cluster. Since the rod clusters are roughly spherical, the clusters will percolate when their volume fraction, ϕ_{cl}, reaches the percolation threshold for random spheres, which is 0.16.[73] If N_{cl} is the number of elements of length L_{eff} in a cluster of size R_{cl}, then percolation occurs when

$$\frac{(4/3)\pi R_{cl}^{3}}{N_{cl}\pi r^2 L_{eff}} \phi_{perc} = 0.16 \tag{18}$$

$$\phi_{perc} = \frac{0.48}{4\alpha_{eff}^{2} N_{cl}^{(3-d_m)/d_m}} \tag{19}$$

where α_{eff} is effective aspect ratio, as described above for the wormlike cluster model.

Unfortunately, we have no morphological data on any system for which the percolation threshold has been measured. To illustrate the impact of clustering, we assume $\alpha_{eff} = 10$, $d_m = 2$, $L_{eff} = 0.5$ μm, and $N_{cl} = 3600$. Using these numbers percolation occurs when at $\phi = 2 \times 10^{-5}$, the value observed by Martin et al. for tubes of native aspect ratio $\alpha = 1 \times 10^3$. Thus, even though the effective aspect ratio is reduced by a factor of 100, clustered nanotubes can percolate at a volume fraction 2 orders of magnitude below that predicted for isolated tubes, for which $\phi_{perc} \cong 1/\alpha = 1 \times 10^{-3}$. If tubes could actually be dispersed as undeformed cylinders, even minor clustering would lead to dramatic reductions in the percolation threshold compared to $1/\alpha$.

5. Conclusions

The scientific literature devoted to nanocomposites is both immense and growing. No report can critically examine the entire canon. We have limited our investigation to an aspect of nanocomposite research that we believe deserves more attention by the nanocomposite community—namely, the large-scale morphology of reinforcing fillers. Because of the difficulty of characterizing the *in situ* structure of nanoscale objects, understanding of filler morphology lags materials development, leading to the proliferation of conflicting claims and little consensus on a global strategy for nanocomposite research or credible end-use targets.

In answer to the question "how nano are nanocomposites?" the answer is "not very". Almost without exception, scattering data show that micron-scale structures are present. This conclusion holds for spherical, rodlike, and sheetlike reinforcing colloidal particles. Surprisingly, these classes of fillers display more similarities than differences. Regardless of the nature of the primary nanoparticle (spheres, rods or sheets), the large-scale morphology is similar. Aggregation is ubiquitous, leading to structures that are more disordered and more flexible than the simple cartoon representations would suggest. The presence of large-scale disorder limits the ability to enhance elastic properties with nanoscale reinforcing fillers. Effective aspect ratios are smaller than that of native particles. In addition, large-scale clusters are more flexible than is generally appreciated. As a result, it is difficult to achieve significant modulus enhancement except in soft materials.

Our perspective suggests alternative research strategies. Since the effective reinforcing element is small in real nanocomposites, high native aspect ratio is not desirable. Large aggregates, long tubes, or large disks are difficult to disperse and end up actually or effectively shortened by harsh dispersion strategies.

We have assumed that nanoscale fillers do not alter the intrinsic properties of the matrix. It is known, however, that colloidal fillers modify cross-linking in rubbers and change T_g in the vicinity of the filler for thermoplastics. Fibers may also act as labile cross-links. [31,32] These factors can alter the mechanical properties more than the elastic properties of the filler,[34] leading to alternative strategies for property enhancement. Such strategies also depend on filler dispersion, however, so the issues raised here may also limit the effectiveness of high surface area fillers.

Hopefully the discussion presented above will convince the reader that large-scale morphology is an important issue in nanocomposite development. There is considerable promise for nanocomposites, but the target applications need to be chosen with some deliberation and fundamental research needs to keep pace with materials development.

Acknowledgment. This work is the result of collaboration with many individuals including Max Belfor, Doug Kohls, Jian Zhao, Chunyan Chen, Rich Vaia, Heather Dowty, Max Alexander, Jeff Baur, Hilmar Koerner, Janis Brown, Tia Benson-Tolle, Dave Anderson, Chenggang Chen, Khalid Lafdi, Karla Strong, Benji Maruyama, Dave Tomlin, Mingshu Yang, Charles Han, Paymen Pakdel, Chetan Suryawanshi, and Raissa Kosso. Some of the data presented are unpublished (Figures 2, 5, and 24). Samples in Figure 2 were prepared and analyzed by Doug Kohls. Samples in Figure 24 were prepared by Hilmar Koerner and Rich Vaia. Samples in Figure 5 were prepared by Chunyan Chen. Figure 23a was measured by Hartmut Fischer on behalf of Southern Clay Products. This research was partially funded by the United States Air Force Research Laboratory through the Wright Brothers Institute and Contract FA8650-50D-5052/0002 with the University of Dayton Research Institute and by the University of Cincinnati.

References and Notes

(1) Vaia, R. A.; Giannelis, E. P. *MRS Bull.* **2001**, *26*, 394−401.
(2) Treacy, M. M. J.; Ebbesen, T. W.; Gibson, J. M. *Nature (London)* **1996**, *381*, 678−680.
(3) Brown, J. M.; Anderson, D. P.; Justice, R. S.; Lafdi, K.; Belfor, M.; Strong, K. L.; Schaefer, D. W. *Polymer* **2005**, *46*, 10854−10865.
(4) Wang, M. J. *Rubber Chem. Technol.* **1998**, *71*, 520−589.
(5) Moniruzzaman, M.; Winey, K. I. *Macromolecules* **2006**, *39*, 5194−5205.
(6) Hussain, F.; Hojjati, M.; Okamoto, M.; Gorga, R. E. *J. Compos. Mater.* **2006**, *40*, 1511−1575.
(7) Gupta, B.; Lacrampe, M. F.; Krawczak, P. *Polym. Polym. Compos.* **2006**, *14*, 13−38.
(8) Zhang, Y. C.; Zhao, Y. H.; Kang, M. Q.; Wang, X. K. *Prog. Chem.* **2006**, *18*, 59−65.
(9) Samir, M.; Alloin, F.; Dufresne, A. *Biomacromolecules* **2005**, *6*, 612−626.
(10) Jordan, J.; Jacob, K. I.; Tannenbaum, R.; Sharaf, M. A.; Jasiuk, I. *Mater. Sci. Eng., A* **2005**, *393*, 1−11.
(11) Ray, S. S.; Okamoto, M. *Prog. Polym. Sci.* **2003**, *28*, 1539−1641.
(12) Huang, Z. M.; Zhang, Y. Z.; Kotaki, M.; Ramakrishna, S. *Compos. Sci. Technol.* **2003**, *63*, 2223−2253.
(13) Manias, E.; Touny, A.; Wu, L.; Strawhecker, K.; Lu, B.; Chung, T. C. *Chem. Mater.* **2001**, *13*, 3516−3523.
(14) Xie, X. L.; Mai, Y. W.; Zhou, X. P. *Mater. Sci. Eng., R* **2005**, *49*, 89−112.
(15) Thostenson, E. T.; Ren, Z.-F.; Chou, T.-W. *Compos. Sci. Technol.* **2001**, *61*, 1899−1912.
(16) Lau, K. T.; Gu, C.; Hui, D. *Composites B* **2006**, *37*, 425−436.
(17) Coleman, J. N.; Khan, U.; Blau, W. J.; Gun'ko, Y. K. *Carbon* **2006**, *44*, 1624−1652.
(18) Schaefer, D. W.; Agamalian, M. M. *Curr. Opin. Solid State Mater. Sci.* **2004**, *8*, 39−47.
(19) Roe, R. J. *Methods of X-ray and Neutron Scattering in Polymer Science;* Oxford University Press: New York, 2000.

(20) Schaefer, D. W.; Kohls, D. J.; Feinblum, E.; Vorobiev, A. New Generation Precipitated Silica For Elastomer Reinforcement. Paper 69, Presented at 170th Technical Meeting, Rubber Division, American Chemical Society, Cincinnati, OH, Oct 10−12, 2006. Available from: Rubber Division, American Chemical Society, Akron, OH.
(21) Schaefer, D. W.; Rieker, T.; Agamalian, M.; Lin, J. S.; Fischer, D.; Sukumaran, S.; Chen, C.; Beaucage, G.; Herd, C.; Ivie, J. *J. Appl. Crystallogr.* **2000**, *33*, 587−591.
(22) Beaucage, G. *J. Appl. Crystallogr.* **1995**, *28*, 717−728.
(23) Guinier, A.; Fournet, G. *Small-Angle Scattering of X-rays;* Wiley: New York, 1955.
(24) Porod, G. *Kolloid-Z.* **1951**, *124*, 83.
(25) Suryawanshi, C. N.; Pakdel, P.; Schaefer, D. W. *J. Appl. Crystallogr.* **2003**, *36*, 573−577.
(26) Kohls, D. J.; Schaefer, D. W.; Feinblum, E.; Vorobiev, A.; Kosso, R. Mechanical Properties of Rubbers Reinforced with Porcellinite-Derived Precipitated Silica. Paper 68, Presented at 170th Technical Meeting, Rubber Division, American Chemical Society, Cincinnati, OH, Oct 10−12, 2006. Available from: Rubber Division, American Chemical Society, Akron, OH.
(27) Schaefer, D. W. *Science* **1989**, *243*, 1023−1027.
(28) Schaefer, D. W.; Chen, C. Y. *Rubber Chem. Technol.* **2002**, *75*, 773−793.
(29) Chen, C. Structure Design and Optimization of Precipitated Silica for Rubber Reinforcement. M.S. Thesis, University of Cincinnati, Cincinnati, OH, 2000.
(30) Smallwood, H. M. *J. Appl. Phys.* **1944**, *15*, 758−766.
(31) Sternstein, S. S.; Zhu, A. J. *Macromolecules* **2002**, *35*, 7262−7273.
(32) Zhu, A. J.; Sternstein, S. S. *Compos. Sci. Technol.* **2003**, *63*, 1113−1126.
(33) Witten, T. A.; Rubinstein, M.; Colby, R. H. *J. Phys. II* **1993**, *3*, 367−383.
(34) Klüppel, M. *Adv. Polym. Sci.* **2003**, *164*, 1−86.
(35) Forsman, J.; Harrison, J. P.; Rutenberg, A. *Can. J. Phys.* **1987**, *65*, 767−771.
(36) Woignier, T.; Phalippou, J.; Vacher, R. *J. Mater. Res.* **1989**, *4*, 688−692.
(37) Schaefer, D. W.; Zhao, J.; Brown, J. M.; Anderson, D. P.; Tomlin, D. W. *Chem. Phys. Lett.* **2003**, *375*, 369−375.
(38) Zhao, C.; Hu, G.; Justice, R.; Schaefer, D. W.; Zhang, S.; Yang, M.; Han, C. C. *Polymer* **2005**, *46*, 5125−5132.
(39) Chen, Q.; Saltiel, C.; Manickavasagam, S.; Schadler, L. S.; Siegel, R. W.; Yang, H. C. *J. Colloid Interface Sci.* **2004**, *280*, 91−97.
(40) Schaefer, D.; Brown, J. M.; Anderson, D. P.; Zhao, J.; Chokalingam, K.; Tomlin, D.; Ilavsky, J. *J. Appl. Crystallogr.* **2003**, *36*, 553−557.
(41) Bauer, B. J.; Hobbie, E. K.; Becker, M. L. *Macromolecules* **2006**, *39*, 2637−2642.
(42) Hobbie, E. K.; Bauer, B. J.; Stephens, J.; Becker, M. L.; McGuiggan, P.; Hudson, S. D.; Wang, H. *Langmuir* **2005**, *21*, 10284−10287.
(43) Fry, D.; Langhorst, B.; Kim, H.; Grulke, E.; Wang, H.; Hobbie, E. K. *Phys. Rev. Lett.* **2005**, *95*.
(44) Zhou, W.; Islam, M. F.; Wang, H.; Ho, D. L.; Yodh, A. G.; Winey, K. I.; Fischer, J. E. *Chem. Phys. Lett.* **2004**, *384*, 185−189.
(45) Hough, L. A.; Islam, M. F.; Hammouda, B.; Yodh, A. G.; Heiney, P. A. *Nano Lett.* **2006**, *6*, 313−317.
(46) Yurekli, K.; Mitchell, C. A.; Krishnamoorti, R. *J. Am. Chem. Soc.* **2004**, *126*, 9902−9903.
(47) Zhao, J.; Schaefer, D. W.; Shi, D.; Lian, J.; Brown, J.; Beaucage, G.; Wang, L.; Ewing, R. C. *J. Phys. Chem. B* **2005**, *109*, 23351−23357.
(48) Justice, R. S.; Wang, D. H.; Tan, L.-S.; Schaefer, D. W. *J. Appl. Crystallogr.*, in press.
(49) Liu, T. X.; Phang, I. Y.; Shen, L.; Chow, S. Y.; Zhang, W. D. *Macromolecules* **2004**, *37*, 7214−7222.
(50) Tucker, C. L.; Liang, E. *Compos. Sci. Technol.* **1999**, *59*, 655−671.
(51) Fukuda, H.; Kawata, K. *Fiber Sci. Technol.* **1974**, *7*, 207−222.
(52) Halpin, J. C. *Primer on Composite Materials Analysis;* Technomic Pub. Co.: Lancaster, PA, 1992.
(53) Thostenson, E. T.; Chou, T. W. *J. Phys. D: Appl. Phys.* **2003**, *36*, 573−582.
(54) Mori, T.; Tanaka, K. *Acta Metall.* **1973**, *21*, 571−574.
(55) Tandon, G. P.; Weng, G. J. *Polym. Compos.* **1984**, *5*, 327−333.
(56) Fornes, T. D.; Paul, D. R. *Polymer* **2003**, *44*, 4993−5013.
(57) Gojny, F. H.; Wichmann, M. H. G.; Fiedler, B.; Schulte, K. *Compos. Sci. Technol.* **2005**, *65*, 2300−2313.
(58) Schmidt, D.; Shah, D.; Giannelis, E. P. *Curr. Opin. Solid State Mater. Sci.* **2002**, *6*, 205−212.
(59) Vaia, R. A.; Liu, W. D.; Koerner, H. *J. Polym. Sci., Part B* **2003**, *41*, 3214−3236.
(60) Ho, D. L.; Briber, R. M.; Glinka, C. J. *Chem. Mater.* **2001**, *13*, 1923−1931.
(61) Tolle, T. B.; Anderson, D. P. *Compos. Sci. Technol.* **2002**, *62*, 1033−1041.
(62) Schaefer, D. W.; Justice, R. S.; Koerner, H.; Vaia, R.; Zhao, C.; Yang, M.; Vale, J. Large-Scale Morphology of Dispersed Layered Silicates. In *Neutron and X-Ray Scattering Probes of Multiscale Phenomena*; Pochan, D., Bhatia, S. R., Khalifah, P. G., Radaelli, R., Eds.; Materials Research Society: Warrendale, PA, 2005; Vol. 840.
(63) Teixeira, J. *J. Appl. Crystallogr.* **1988**, *21*, 781−785.
(64) Drummy, L. F.; Koerner, H.; Farmer, K.; Tan, A.; Farmer, B. L.; Vaia, R. A. *J. Phys. Chem. B* **2005**, *109*, 17868−17878.
(65) Pandey, R. B.; Anderson, K. L.; Farmer, B. L. *J. Polym. Sci., Part B* **2005**, *43*, 3478−3486.
(66) Fischer, H. *Mater. Sci. Eng., C* **2003**, *23*, 763−772.
(67) Sheng, N.; Boyce, M. C.; Parks, D. M.; Rutledge, G. C.; Abes, J. I.; Cohen, R. E. *Polymer* **2004**, *45*, 487−506.
(68) Yung, K. C.; Wang, J.; Yue, T. M. *J. Reinf. Plast. Compos.* **2006**, *25*, 847−861.
(69) Gusev, A. A. *Macromolecules* **2001**, *34*, 3081−3093.
(70) Fornes, T. D.; Paul, D. R. *Macromolecules* **2004**, *37*, 7698−7709.
(71) Martin, C. A.; Sandler, J. K. W.; Shaffer, M. S. P.; Schwarz, M. K.; Bauhofer, W.; Schulte, K.; Windle, A. H. *Comp. Sci. & Tech.* **2004**, *64*, (15), 2309−2316.
(72) Celzard, A.; McRae, E.; Deleuze, C.; Dufort, M.; Furdin, G.; Mareche, J. F. *Phys. Rev. B* **1996**, *53*, 6209−6214.
(73) Pike, G. E.; Seager, C. H. *Phys. Rev. B* **1974**, *10*, 1421.
(74) Koerner, H.; Liu, W. D.; Alexander, M.; Mirau, P.; Dowty, H.; Vaia, R. A. *Polymer* **2005**, *46*, 4405−4420.
(75) Vale, J. M.; Justice, R. S.; Schaefer, D. W.; Mark, J. E. *J. Macromol. Sci., Phys. Ed.* **2005**, *44*, 1−11.

MA070356W